Tracing immune cells around biomaterials with spatial anchors during wound regeneration

Authors: Yang Yang[1]†, Chen-yu Chu[1]†, Yi Man[1]†, Li Liu[1]†, Chen-bing Wang[1], Chen Hu[1], Xin-hui Li[1], Yi-li Qu[1]*

Affiliations:

[1] Department of Oral Implantology &State Key Laboratory of Oral Diseases & National Clinical Research Center for Oral Diseases, West China Hospital of Stomatology, Sichuan University; Chengdu 610041, China.

* Corresponding author. Email: qqyili@126.com (Y.L.Q.)

† These authors contributed equally to this work

Abstract: Generally, only a few hair follicles (HF) regenerate upon severe wounds in adult mammals which restricted to the large wound center, termed as wound-induced hair follicle neogenesis (WIHN). We observed enhanced WIHN with implantation of extracellular matrix scaffolds, regardless of wound size. Paired analysis of single-cell RNA with spatial resolution during wound regeneration provides a unique lens through which we can explore delicate cellular interactions. The spatial anchor highlights preferential aggregation of adaptive immune cells in large wound centers colocalized with HF precursor cells. Recruited adaptive immune cells surrounding biomaterials may exert a further pro-regenerative effect on HF neogenesis. Immunodeficient mice lacking mature adaptive immune cells lost the ability to stimulate WIHN, validating the potential therapeutic effect of the adaptive immune system in appendage regeneration.

One-Sentence Summary: Multimodal analysis tracing the regenerative effect of the adaptive immune system activated by biomaterials during wound healing.

Main Text: Extracellular matrix (ECM) scaffolds are an efficient treatment for severe wounds (*1*) but still lack the ability to stimulate hair follicle (HF) neogenesis (*2*). Intriguingly, a rare capability for HF regeneration has been observed in large full-thickness wound centers in the wound-induced hair follicle neogenesis (WIHN) model (*3, 4*). It has been suggested that immune cells (mainly macrophages and T cells) might be the key orchestrators of wound healing that selectively promote scarring (*5-7*) or regenerative WIHN (*8-11*), but the spatial heterogeneity of immune systems remains unclear. Biological cues can be integrated into a polymer scaffold to mimic the native ECM, which guides immune cell activity (*12, 13*). Our previous study showed that the Aligned ECM scaffold could lead to enhanced regeneration of HF along with an immunomodulatory effect (*14, 15*). However, the spatial distribution of the immune cells at the single-cell RNA transcriptome level remains unclear. First, a circular splinted excisional wound healing model was used to evaluate the relationship between wound size and HF regeneration. We found that a diameter of 1.5 cm was the critical threshold for stimulating WIHN, marked by de novo HF regeneration restricted to the wound center. Next, we noticed that the ECM scaffold exerted a further pro-regenerative effect on enhancing de novo HF regeneration. Multiomic approaches, including single-cell RNA-sequencing (scRNA-seq) and spatial transcriptomics (ST), were applied to trace cell heterogeneity in the area of interest. Unveiling the immune cell composition around biomaterials provided a further understanding of the foreign body response (FBR) and anchored the key role of adaptive immune cells in HF regeneration. Finally, we observed that immunodeficient mice lacking mature T lymphocytes and functional macrophages were unable to stimulate HF regeneration, which confirmed that the adaptive immune system activated by biomaterials was crucial for scarless wound healing.

Results

WIHN model construction

We created circular wounds of different diameters in a murine splinted full-thickness excisional wound healing model (Fig. 1A). By comparing the de novo HF number, we confirmed the threshold value (diameter = 1.5 cm) for triggering the WIHN phenomenon (Fig. 1B). To explore the underlying mechanism, we created a small wound (diameter = 0.6 cm) in the Ctrl_SW group and a large wound (diameter = 1.5 cm) in the Ctrl_LW group (Fig. 1C). Wound tissue was harvested for further examination (Fig. 1D). Based on the bulk-tissue RNA sequencing (bulk-seq) profile, we observed that the large wound showed upregulated gene expression, enrichment in hair follicle development, and αβT cell differentiation (Fig. 1E). The correlation heatmap also showed a positive correlation between HF regeneration-related genes and adaptive immune response-related genes (Fig. 1F). Immunofluorescence (IF) staining (Fig. 1G) and flow cytometry (Fig. 1H) confirmed that large wounds (especially wound centers) maintained substantial adaptive T cell infiltration.

Tracing the distribution of single cells in the WIHN model

To explore the spatial characteristics of single cells during wound healing, we applied ST and scRNA-seq to compare the spatial gene expression profiles between small and large wounds (Fig. 2A). The single-cell annotation process is shown in the Supplementary Materials (fig. S1-S4). We observed a higher proportion of HF precursor cells, including hair follicle progenitors (HFP) (*16*), hair follicle stem cells (HFSC) (*8*) and papillary fibroblasts (PF) (*17*, *18*), in the Ctrl_LW group (fig. S2 C and G). The anatomical structures of the wounds could be clearly distinguished based on the ST profile (Fig. 2 B and C). Scoring spots in each section with marker genes from scRNA-seq showed that PF (HF-related) exhibited strong spatial preferences within the large wound center (Fig. 2D), which may account for subsequent HF regeneration. In

contrast, reticular fibroblasts (RF) and lipofibroblasts (LF), in relation to collagen deposition, are the dominant subtypes driving small wound healing (Fig. 2F), which might explain why small wounds generally heal with scarring devoid of HF. Gene enrichment analysis showed that the Ctrl_LW sample upregulated genes related to hair follicle morphogenesis and antigen presentation (Fig. 2C). Sub-clustering analysis of ST showed that these genes were preferentially expressed in large wound center and margin (fig. S5–S6).Feature plot showed the aggregation of *Ptprc*+ immune cells (Fig. 2D). To explore how distinct immune cell types may contribute to the regeneration process, the heterogeneity of immune cell sub-clusters was evaluated. As shown in Fig. 2 G and H, monocytes (Mono), pro-inflammatory macrophages (PIM), and anti-inflammatory macrophages (AIM) were diffusely distributed in small wounds, whereas Mono (related to antigen presentation) and PIM (related to pro-inflammatory pathways) showed preferential aggregation in the large wound center. In addition, the Ctrl_LW group showed a higher proportion of adaptive T-cells. Almost all T cell sub-clusters were exclusively expressed in the large wound center. In contrast, there seems to be a lack of observable T-cell infiltration in small wounds (Fig. 2 I and J). To summarize, it was in large wound that we observed the preferential aggregation of PF (HF-related) as well as adaptive T cells, Mono and PIM, which laid the foundation of potential cellular communication among them.

Cellular communication landscape between immune cell and HF-related cutaneous cell

Next, to address the potential interactions between the defined cell sub-clusters (fig. S2–S4), especially co-localized subpopulations, including PF and adaptive immune cells (fig. S7 A and B), CellChat (*19*) was used to predict cell-cell communication patterns at the level of ligand/receptor expression. We selected upregulated pathways and compared the overall signaling strength of ligand receptors that exhibited different signaling patterns (fig. S7C). Adaptive immune system-related pathways, including MHC-I, MHC-II, and CD80, were

exclusively enriched in the large wounds. The major signaling among immune and cutaneous cells in large wounds is mediated by PF (HF-related). As shown in fig. S7D, adaptive immune cells and hair follicle precursor cells were enriched with interacting ligand or receptor gene partners such as IL6/IL6ST and INHBA/Acvr1b. Spatial plots showed preferential aggregation of IL6 and INHBA in large wounds. The essential roles of activin (*20, 21*) and IL6 (*10*) pathways in HF regeneration have been reported. Our results suggest that immune cells, especially T cells, Mono, and PIM, may modulate the state of PF, hair follicle progenitor (HFP), and hair follicle stem cells (HFSC) through signaling pathways such as IL-6 and activin.

Enhanced WIHN occurs in scaffold-implanted wounds with further activation of the adaptive immune system

Synthetic graft transplantation is an efficient treatment for severe large-area skin wounds, especially when the donor site is not qualified (*1*). With additional understanding of tissue engineering, it is suggested that synthetic biomaterials imitating the native structure of ECM can integrate and potentially play a pro-regenerative role in wound healing (*12, 22*). Our previous report illustrated the immunoregulatory effect of ECM scaffolds in small wound (diameter = 0.6 cm) healing (*14, 15*). Next, we repeated a large full-thickness wound-healing model in C57BL/6 mice with or without implanted biomaterial to investigate whether a further regenerative phenomenon was observed in ECM scaffold-treated wounds. The workflow for evaluating large wound healing is summarized in Fig. 3A. We placed ECM scaffolds below the large wound (diameter = 1.5 cm; Fig. 3B) in the ECM_LW group, while the Ctrl_LW group received no biomaterials. Wound coverage was faster in the ECM_LW group (Fig. 3C and D), and the ECM_LW group also had a smaller gap width (Fig. 3E and G). IF staining for cytokeratin 5 (Krt5) and cytokeratin 10 (Krt10) showed that keratinocytes crawled around the biomaterials (Fig. 3I), and the ECM_LW group had a larger area of neoepithelium (Fig. 3J). As shown in Fig.

3F, the ECM membrane implanted in the large wound did not trigger any obvious fibrous capsule and exhibited a rapid degradation rate in vivo. We observed degrading fragments on POD14 and degrading particles on POD21, and there were no visible particles remaining on POD28. In addition, the outline of HF morphogenesis could be recognized in the ECM_LW group; with the first appearance in the hair germ stage on POD7, they gradually grew into a bulbous-peg structure overlaying the degrading scaffold fragments on POD21. On POD28, we found that the ECM_LW group recapitulated the normal skin architecture with an equivalent number of mature appendages and "basket-wave" ECM collagen deposition (Fig. 3H). In summary, in a large full-thickness mouse wound model, the biomaterial led to faster wound healing and enhanced the regeneration of HF. The excellent biocompatibility and degradability of the membrane also prevented the risk of immune rejection and secondary surgery in further clinical applications. To explore the underlying mechanism, we noticed that the ECM_LW group showed increased enrichment of genes involved in hair follicle development and T cell differentiation (Fig. 3K). Immunohistochemistry (IHC) staining and flow cytometry confirmed increased T-cell infiltration around the implanted biomaterials (Fig. 3 L and M).

Discovery of spatial heterogeneity around biomaterials at single-cell resolution

To explore the spatial characteristics of cell heterogeneity in scaffold-implanted wounds, we applied ST and scRNA-seq to analyze the spatial gene expression profiles (Fig. 4A). Anatomical structures were also identified in the ST sections (Fig. 4 C and D). The single-cell annotation process is shown in the Supplementary Materials (fig. S8-S11). Based on the scRNA-seq analysis, the ECM_LW group had a higher proportion of HF precursor cells (Fig. 4F). The spatial feature plot illustrated keratinocytes crawling around the implanted biomaterials (Fig. 4E). Moreover, the distribution of PF (HF-related) was enlarged in the ECM_LW group. In contrast, lower lineage fibroblasts, including RF and LF (related to collagen deposition), were

significantly reduced (Fig. 4 G and H), suggesting different healing outcomes of two groups. Generally, HF formation does not start until several days after wound closure in large wounds without implantation (POD14–21) (*3*). In the ST profiling of the ECM_LW group on POD7, we identified the initial structure of the HF composed of Krt28^{+}HFP in the neo-epidermis and Twis2^{+} dermal condensate (Dc) aggregation beneath the dermis (Fig. 4I), which highlighted the early HF formation signature in the ECM_LW group at the spatial gene expression level (Fig. 4J). Feature plot showed the aggregation of *Ptprc*+ immune cells (Fig. 4B). Based on the gene enrichment analysis of ST, the ECM_LW sample showed upregulated gene expression in hair follicle morphogenesis as well as an adaptive immune response (Fig. 4D). To explore the scaffold-induced immune microenvironment, we integrated marker genes of immune cells (defined in fig. S9–S10) with ST profiling. We noticed an obvious aggregation of monocyte-macrophages (MAC) and T cells surrounding the biomaterial (Fig. 4K-4N). Notably, we observed the accumulation of tissue-resident (innate lymphoid cell) ILC in the epithelium and granulation tissue in the ECM_LW group (Fig. 4M). ILCs that co-expressed genes related to the adaptive immune response as well as hair follicle development may be critical regulators initiating HF formation.

Prediction of critical signaling patterns between spatially co-localized cell populations around the biomaterial

Based on the multimodal profiling, we still observed the overlapping distribution of adaptive and HF precursor cells in the ECM_LW group, which implied a potential cellular communication among them. Next, we applied CellChat to predict the cell-cell communication patterns between EMC_LW and Ctrl_LW (Fig. 5A and B). The heatmap shows the overall signaling strength of the ligand receptors in the Ctrl_LW and ECM_LW groups (Fig. 5C). Adaptive immune system-related pathways, including MHC-II, were further activated in ECM_LW. In addition to IL6, key

signaling pathways in embryonic HF development, such as fibroblast growth factor (FGF) (*23*), Notch (*24*), and KIT (*19*) were also upregulated in the ECM_LW group. Consistent with the ST profiles, adaptive immune cells and HF precursor cells were enriched with interacting receptor/ligand gene partners, including Areg-(Egfr+Erbb2), Epgn-Egfr, Mdk-(Sdc1 or Itgb1), and Ptn-(Itgb1or Sdc1) (Fig. 5D and E). The critical functions of epidermal growth factor (EGF) (*25*), pleiotrophin (PTN), and midkine (MK) (*19*) in skin morphology have been previously emphasized. Based on our analysis, adaptive immune cells might modulate HF precursor cell growth through these pathways, thus facilitating HF formation. To test the role of adaptive immune system in HF regeneration, we placed ECM scaffolds in the dorsal skin of immunodeficient C57Bl/6 (B6.129-Rag2tm1) mice, which lacked mature T lymphocytes and functional macrophages(*26, 27*) (Fig. 5 F and G). We noticed that the wound closure rate was delayed in Rag2$^{-/-}$ mice (Fig. 5H–5J) and regeneration of HF was scarce in Rag2$^{-/-}$ mice (Fig. 5K). Compared to wild type (WT) mice that recruited plenty Cd3^{+} T cells and Cd68^{+} macrophages surrounding biomaterials, we observed obvious aggregation of Ly6g^{+} neutrophils in Rag2$^{-/-}$ mice instead (Fig. 5 L and M). It is necessary to elucidate the mechanisms underlying mature T cell regulation of neutrophil homeostasis further.

Biomaterials facilitate de novo HF regeneration despite of wound size

To detect any differences in wound healing between small and large wounds treated with biomaterials, we repeated the experiment with small (diameter=0.6 cm) and large (diameter=1.5 cm) full-thickness wounds implanted with biomaterials (Fig. 6 A and B). Consistent with the ECM_LW group, the scaffold implanted in the small wound did not trigger an obvious FBR fibrous capsule and had a rapid degradation rate (Fig. 6 C and D). Histological sections of ECM_SW tissue revealed clear signs of enhanced WIHN (Fig. 6 C and F). Based on bulk-seq profiling, heatmaps showed insignificant changes in HF-related gene expression, adaptive

immune response, or innate immune response between the two groups (fig. S12A). IHC staining for Cd3 and Cd68 confirmed similar infiltration levels of T cells and macrophages surrounding the scaffold or in the granulation tissue (Fig. 6E). We further explored the differences in immune cell composition using scRNA-seq and ST (Fig. 6 G and H). Feature plot showed the aggregation of *Ptprc*+ immune cells (Fig. 6I). The total proportion of MAC was in equilibrium between the two groups (fig. S12B), and integrated analysis of ST profiling showed similar distributions of the three MAC subsets around the scaffold (Fig. 6 J and K). Integrated analysis confirmed the substantial distribution of T cell subsets surrounding the scaffold in both the groups (Fig. 6 L and M). In summary, the biomaterial showed similar "pro-regenerative" effect on wound healing despite the wound size. In addition, this resemblance to the immunoregulatory effect of the adaptive immune system indicates a significant role of modulating the immune environment in HF regeneration.

Discussion

Problems such as delayed wound closure, susceptibility to infection, and inability to regenerate appendages have become the main impediments to skin wound healing (*28*). Requirements for promotion of nascent HF formation bring significant challenges to biomaterial design, particularly for large-scale, full-thickness wounds. WIHN is a rare model of mammalian organ regeneration in adult mice, wherein a large full-thickness wound (>1cm^2) induces little nascent HF regeneration limited to the wound center (*3*). The initiation of HF morphogenesis begins when the HFP (*16*) and HFSC (*8*) migrate to the neo-epithelium and induce the aggregation of Dc (derived from PF) under them (*29*). The pro-regenerative influence of the immune system in coordinating the early stages of wound repair has been stressed (*30*). However, the cellular interplay between specific immune sub-clusters and HF precursor cells remains unclear. Here, we first compared the transcriptomic profiles of the total "scarring" (Ctrl_SW, diameter = 0.6

cm) and “half-regenerative” WIHN (Ctrl_LW, diameter = 1.5 cm) models. From our multimodal analysis, we first observed a higher proportion of adaptive immune cells in the WIHN group (Fig. 2 G and I), which resided in large wound centers co-localized with HF precursor cells (Fig. 2 F and H). The active regional cell-cell communications among them indicated the “pro-regenerative” role of adaptive immune cells in promoting HF neogenesis and served as a promising therapeutic target for the application of immunoregulatory materials in skin wound regeneration (fig. S7). Next, we employed an ECM scaffold for large-area skin defects and investigated its role in wound healing and modulation of the immune microenvironment. The scaffold showed an impact by accelerating wound closure and promoting nascent HF formation (Fig. 3 E and H). It has been shown that biomaterials have a regulatory effect on the adaptive immune system. We found that substantial T cell infiltration in response to scaffold implantation was driven towards regenerative subpopulations (Fig. 4L), overlapping with the abundant PF (HF-related) (Fig. 4F). The local intercellular communications among the enlarged “pro-regenerative” immune niche and HF precursor cells supported the essential role of the adaptive system in biomaterial-mediated HF regeneration (Fig. 5 D and E). Meanwhile, mild FBR around the scaffold decreased the risk of immune rejection, and the appropriate degradation rate could also avoid the extra expense of secondary surgery. In this study, we first defined the spatial heterogeneity of a single cell during biomaterial-mediated wound regeneration. These approaches provide a unique medium through which we can further understand the delicate immunoregulatory mechanisms of biomaterials. Taken together, this study offers a method to regenerate skin appendages with severe damage by modulating the adaptive immune system, and provides further insights into the future design of targeted immunoregulatory materials for scarless wound regeneration.

References and Notes

1. D. Henn *et al.*, Xenogeneic skin transplantation promotes angiogenesis and tissue regeneration through activated Trem2(+) macrophages. *Science advances* **7**, eabi4528 (2021).doi:10.1126/sciadv.abi4528
2. M. Kurita *et al.*, In vivo reprogramming of wound-resident cells generates skin epithelial tissue. *Nature* **561**, 243-247 (2018).doi:10.1038/s41586-018-0477-4
3. M. Ito *et al.*, Wnt-dependent de novo hair follicle regeneration in adult mouse skin after wounding. *Nature* **447**, 316-320 (2007).doi:10.1038/nature05766
4. M. V. Plikus *et al.*, Regeneration of fat cells from myofibroblasts during wound healing. *Science (New York, N.Y.)* **355**, 748-752 (2017).doi:10.1126/science.aai8792
5. I. C. Boothby, J. N. Cohen, M. D. Rosenblum, Regulatory T cells in skin injury: At the crossroads of tolerance and tissue repair. *Science immunology* **5**, (2020).doi:10.1126/sciimmunol.aaz9631
6. B. A. Shook *et al.*, Myofibroblast proliferation and heterogeneity are supported by macrophages during skin repair. *Science (New York, N.Y.)* **362**, (2018).doi:10.1126/science.aar2971
7. D. Gay *et al.*, Phagocytosis of Wnt inhibitor SFRP4 by late wound macrophages drives chronic Wnt activity for fibrotic skin healing. *Science advances* **6**, eaay3704 (2020).doi:10.1126/sciadv.aay3704
8. X. Wang *et al.*, Macrophages induce AKT/β-catenin-dependent Lgr5(+) stem cell activation and hair follicle regeneration through TNF. *Nature communications* **8**, 14091 (2017).doi:10.1038/ncomms14091
9. D. Gay *et al.*, Fgf9 from dermal γδ T cells induces hair follicle neogenesis after wounding. *Nature medicine* **19**, 916-923 (2013).doi:10.1038/nm.3181
10. A. M. Nelson *et al.*, Interleukin-6 Null Mice Paradoxically Display Increased STAT3 Activity and Wound-Induced Hair Neogenesis. *The Journal of investigative dermatology* **136**, 1051-1053 (2016).doi:10.1016/j.jid.2015.12.043
11. P. Lee *et al.*, Stimulation of hair follicle stem cell proliferation through an IL-1 dependent activation of γδT-cells. *eLife* **6**, (2017).doi:10.7554/eLife.28875
12. B. Yi, Q. Xu, W. Liu, An overview of substrate stiffness guided cellular response and its applications in tissue regeneration. *Bioactive materials* **15**, 82-102 (2022).doi:10.1016/j.bioactmat.2021.12.005
13. K. Sadtler *et al.*, Design, clinical translation and immunological response of biomaterials in regenerative medicine. *Nature Reviews Materials* **1**, 16040 (2016).doi:10.1038/natrevmats.2016.40
14. C. Hu *et al.*, Dissecting the microenvironment around biosynthetic scaffolds in murine skin wound healing. *Science advances* **7**, (2021).doi:10.1126/sciadv.abf0787
15. C. Wang *et al.*, The diameter factor of aligned membranes facilitates wound healing by promoting epithelialization in an immune way. *Bioactive materials* **11**, 206-217 (2022).doi:10.1016/j.bioactmat.2021.09.022
16. M. W. Hughes *et al.*, Msx2 Supports Epidermal Competency during Wound-Induced Hair Follicle Neogenesis. *The Journal of investigative dermatology* **138**, 2041-2050 (2018).doi:10.1016/j.jid.2018.02.043

17. S. Abbasi *et al.*, Distinct Regulatory Programs Control the Latent Regenerative Potential of Dermal Fibroblasts during Wound Healing. *Cell stem cell* **27**, 396-412.e396 (2020).doi:10.1016/j.stem.2020.07.008
18. S. B. Telerman *et al.*, Dermal Blimp1 Acts Downstream of Epidermal TGFβ and Wnt/β-Catenin to Regulate Hair Follicle Formation and Growth. *The Journal of investigative dermatology* **137**, 2270-2281 (2017).doi:10.1016/j.jid.2017.06.015
19. S. Jin *et al.*, Inference and analysis of cell-cell communication using CellChat. *Nature communications* **12**, 1088 (2021).doi:10.1038/s41467-021-21246-9
20. W. Wang *et al.*, Changes in regeneration-responsive enhancers shape regenerative capacities in vertebrates. *Science (New York, N.Y.)* **369**, (2020).doi:10.1126/science.aaz3090
21. C. Seo, M. Kwack, M. Kim, J. Kim, Y. Sung, Activin A-induced signalling controls hair follicle neogenesis. *Experimental dermatology* **26**, 108-115 (2017).doi:10.1111/exd.13234
22. M. Monavarian, S. Kader, S. Moeinzadeh, E. Jabbari, Regenerative Scar-Free Skin Wound Healing. *Tissue engineering. Part B, Reviews* **25**, 294-311 (2019).doi:10.1089/ten.TEB.2018.0350
23. K. Mok *et al.*, Dermal Condensate Niche Fate Specification Occurs Prior to Formation and Is Placode Progenitor Dependent. *Developmental cell* **48**, 32-48.e35 (2019).doi:10.1016/j.devcel.2018.11.034
24. N. Ali *et al.*, Regulatory T Cells in Skin Facilitate Epithelial Stem Cell Differentiation. *Cell* **169**, 1119-1129.e1111 (2017).doi:10.1016/j.cell.2017.05.002
25. A. Nosbaum *et al.*, Cutting Edge: Regulatory T Cells Facilitate Cutaneous Wound Healing. *Journal of immunology (Baltimore, Md. : 1950)* **196**, 2010-2014 (2016).doi:10.4049/jimmunol.1502139
26. K. Sadtler *et al.*, Developing a pro-regenerative biomaterial scaffold microenvironment requires T helper 2 cells. *Science (New York, N.Y.)* **352**, 366-370 (2016).doi:10.1126/science.aad9272
27. J. C. Doloff *et al.*, Colony stimulating factor-1 receptor is a central component of the foreign body response to biomaterial implants in rodents and non-human primates. *Nat Mater* **16**, 671-680 (2017).doi:10.1038/nmat4866
28. S. Mascharak *et al.*, Preventing Engrailed-1 activation in fibroblasts yields wound regeneration without scarring. *Science (New York, N.Y.)* **372**, (2021).doi:10.1126/science.aba2374
29. V. Thulabandu, D. Chen, R. P. Atit, Dermal fibroblast in cutaneous development and healing. *Wiley interdisciplinary reviews. Developmental biology* **7**, (2018).doi:10.1002/wdev.307
30. G. Wang *et al.*, Bacteria induce skin regeneration via IL-1β signaling. *Cell host & microbe* **29**, 777-791.e776 (2021).doi:10.1016/j.chom.2021.03.003

Acknowledgments: We thank the Novogene company for RNA sequencing work, and the National Clinical Research Center for Oral Diseases & State Key Laboratory of Oral Diseases

for animal experiment, and the Analytical & Testing Center of Sichuan University for the fabrication of biomaterials. We thank Jia-yu Gao and Sheng-an Rung for the help with analysis.

Funding: Sichuan Science and Technology Plan grant 2022YFS0041 (Y.L.Q.)

Interdisciplinary Innovation Project, West China Hospital of Stomatology Sichuan University grant RD-03- 202006 (Y.M.)

Research and Develop Program, West China Hospital of Stomatology Sichuan University grant LCYJ2019-19 (Y.M.)

Author contributions:

Conceptualization: YY, CYC

Methodology: CYC, LL, CH, CBW

Investigation: YY, XHL

Visualization: YY

Writing – original draft: YY

Writing – review & editing: CCY

Funding acquisition & Project administration & Supervision: YM, YLQ, CCY

Competing interests: Authors declare that they have no competing interests.

Data and materials availability: All data to support the conclusions in this manuscript can be found in the figures and the supplementary materials. Any other data can be requested from the corresponding authors.

Supplementary materials:

Materials and Methods

Supplementary Text

Figs. S1 to S12

References (*31–##*)

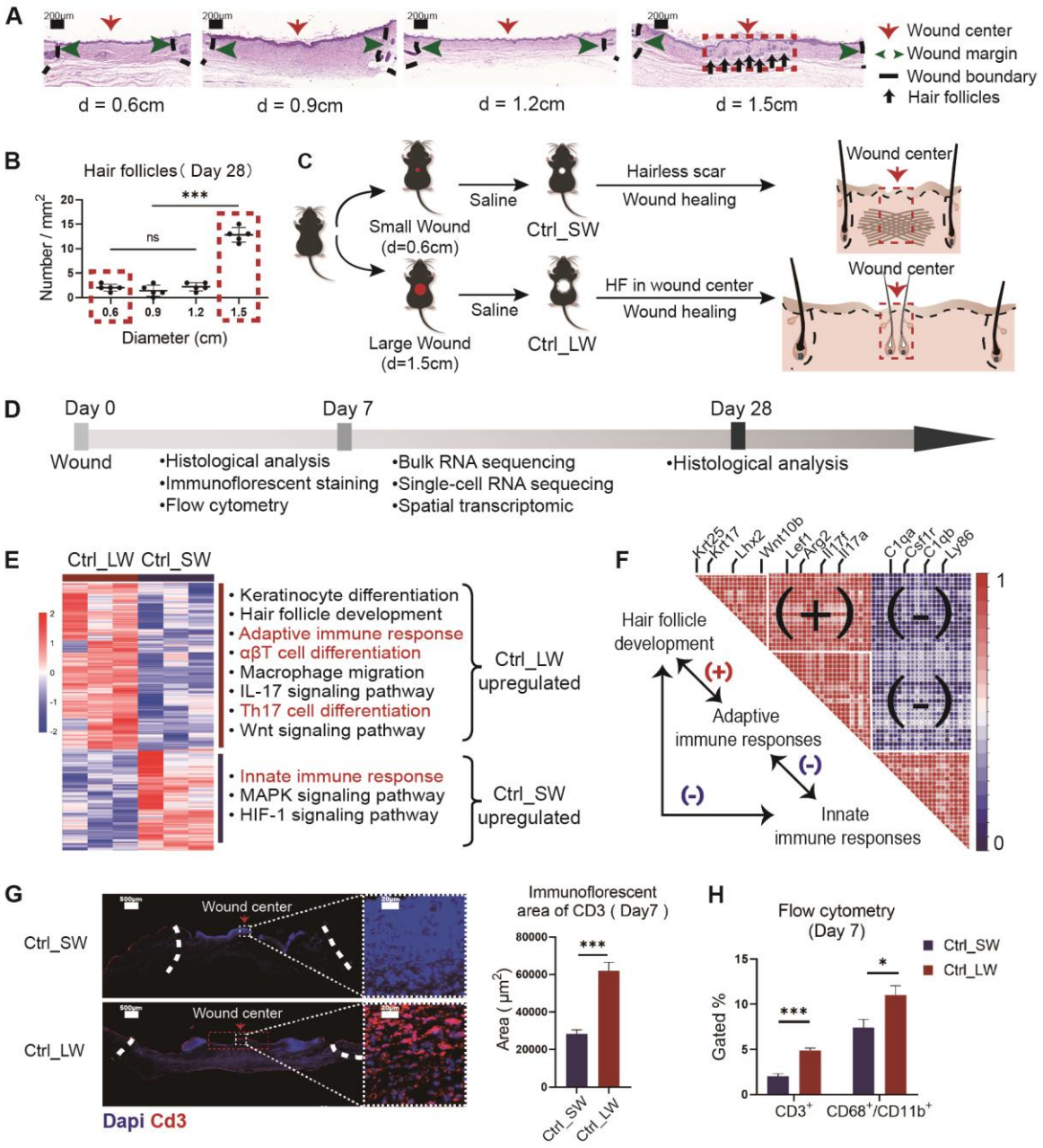

Fig. 1. Evaluation of the healing of small and large full-thickness wound. (A) Haematoxylin and eosin (H&E) staining evaluating skin wound healing outcomes of different wound size. (B) Histologic quantification of de novo hair follicles. (C) Surgical process for the mice full-thickness excisional splinted of small (Ctrl_SW) and large (Ctrl_LW) wound and different healing outcomes. (D) Workflow for evaluating mice skin wound healing of different wound size. (E) Heatmap showing hierarchical clustering of differentially expressed genes (p value<0.05 & |log2FC|> 1) , and gene set enrichment analysis showing the up-regulated GO

terms and KEGG pathways between two groups. (F) Pearson correlation analysis shows relation between the gene expression of hair follicle development related genes, adaptive immune responses related genes and innate immune responses related genes (positive, red; negative, blue). (G) IF staining of Cd3 (red) in histologic sections and corresponding quantification. (H) In vivo flow cytometry strategy using Cd3 to identify T cells; monocyte, and macrophages co-expressing the surface markers CD68 and CD11b, and the corresponding quantification.

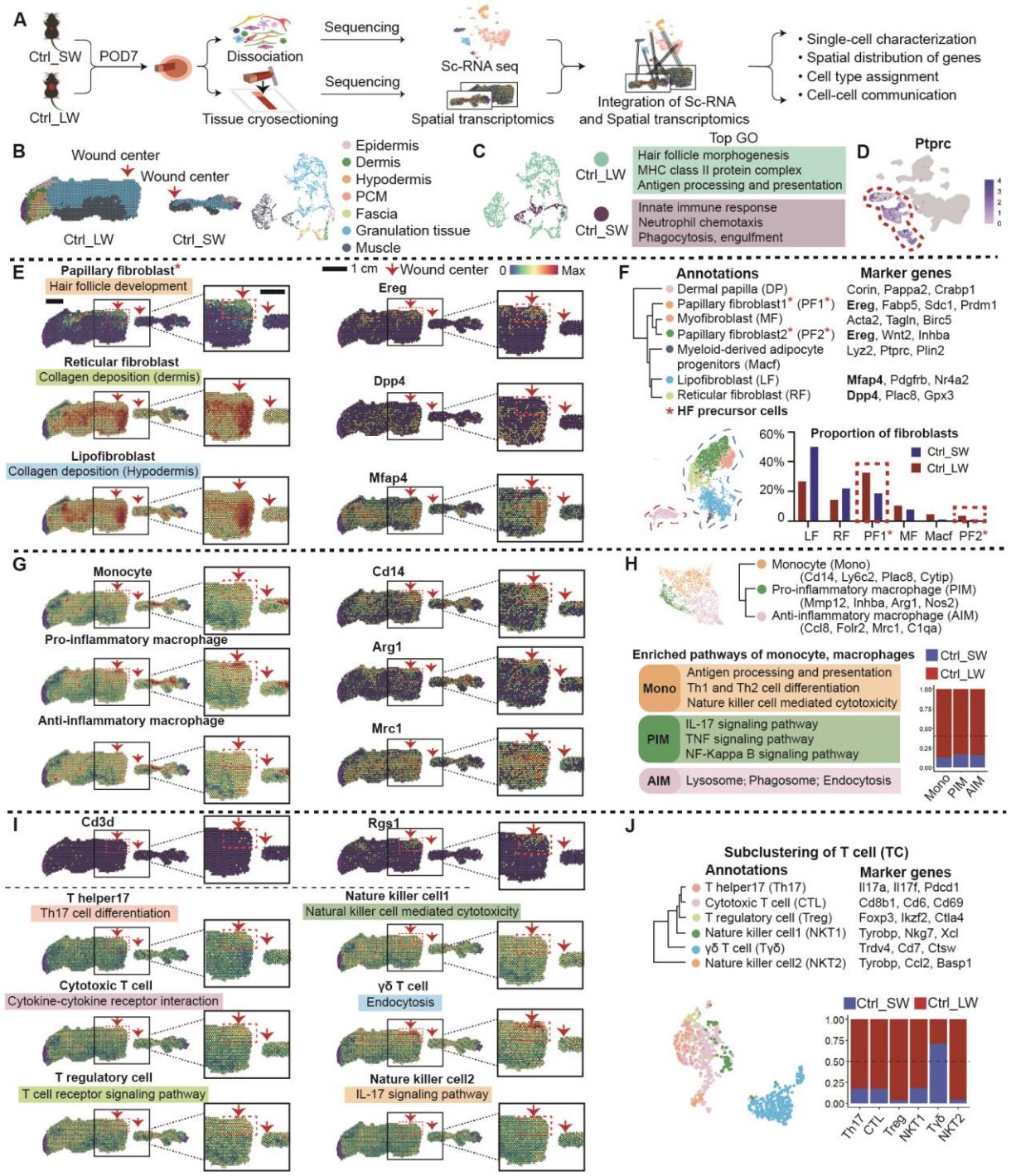

Fig. 2. Spatial transcriptomics applied to Ctrl_SW and Ctrl_LW. (A) Schematic for generating sc-RNA seq and spatial transcriptomics data from splinted excisional wounds. (B) Spatial plots and UMAP plot showing that the anatomical regions could be distinguished by their transcriptional programs. (C) Gene enrichment analysis between Ctrl_SW and Ctrl_LW. (D) Feature plot showed the expression of Ptprc (Cd45) in scRNA-seq dataset. (E) Spatial feature

plots showed defined fibroblast subclusters distribution in tissue sections. (F) Subclustering of fibroblast in sc-RNA seq dataset. (G) Spatial feature plots showed defined MAC subclusters distribution in tissue sections. (H) Subclustering of MAC in sc-RNA seq dataset. (I) Spatial feature plots showed expression of Cd3d and Rgs1 (marker genes of TC and defined TC subclusters distribution in tissue sections. (J) Subclustering of TC in Sc-RNA seq dataset.

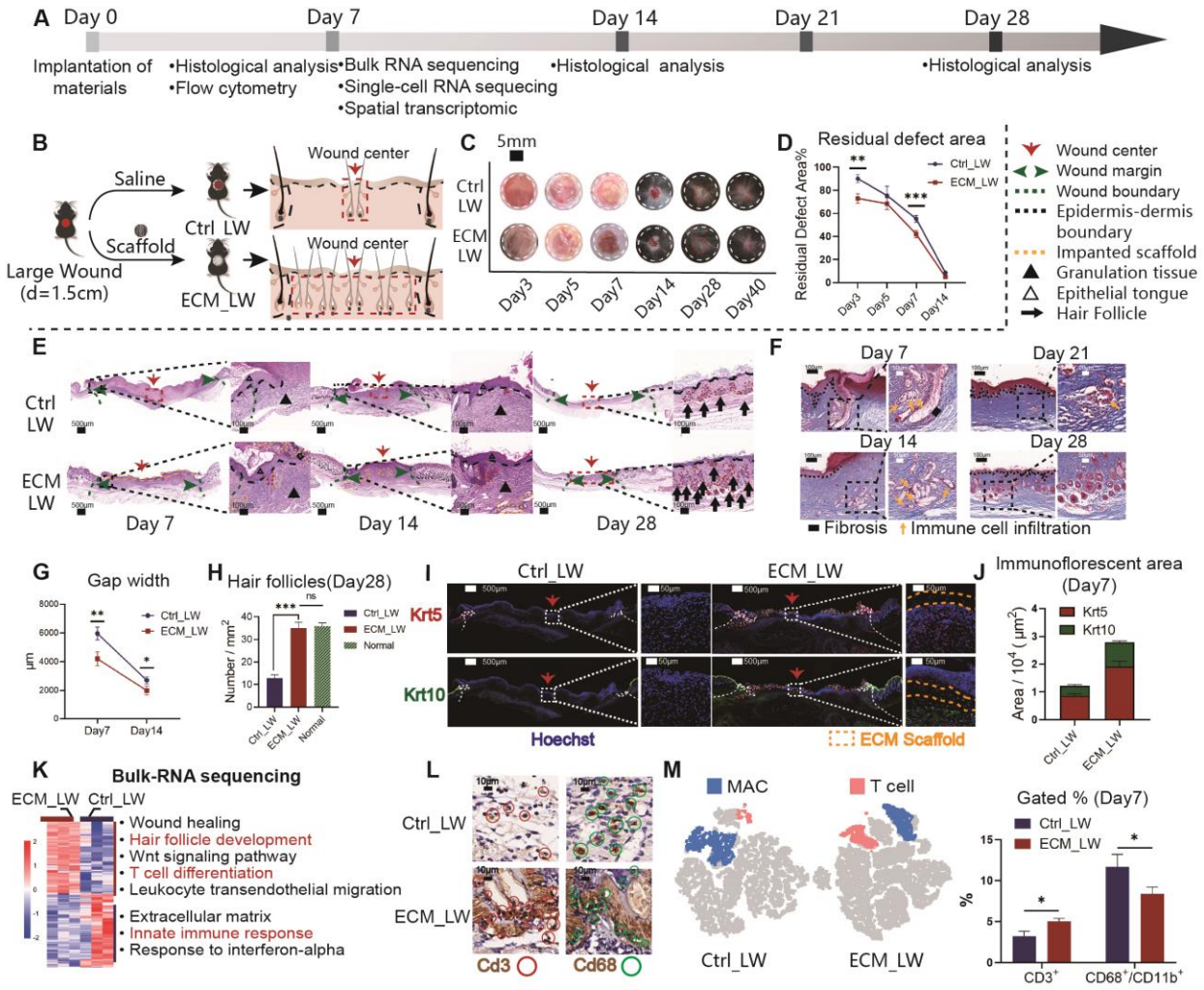

Fig. 3. Evaluation of the healing of large full-thickness wounds with/without implanted ECM scaffolds. (A) Workflow for evaluating large-scale wound healing. (B) Surgical processes for skin excisional wound model. (C) Residual wound area at 3, 5, 7, 14 and 28 days, and (D) corresponding analysis. (E) H&E analysis of two groups. (F) Evaluation of FBR around the biomaterials. Masson's trichrome staining for ECM_LW group at 7, 14, 21 and 28 days. (G) Semiquantitative evaluation of gap width. (H) Histologic quantification of de novo HFs on POD28. (I) IF staining using Krt5 (red) and Krt10 (green) and (J) semiquantitative evaluation of the fluorescent area. (K) Heatmap showing hierarchical clustering of differentially expressed genes (p value<0.05 & |log2FC|> 1) and gene set enrichment analysis. (L) IHC staining of Cd3 and Cd68. (M) In vivo flow cytometry strategy using Cd3 to identify T cells; Monocyte-macrophages co-expressing the surface markers CD68 and CD11b.

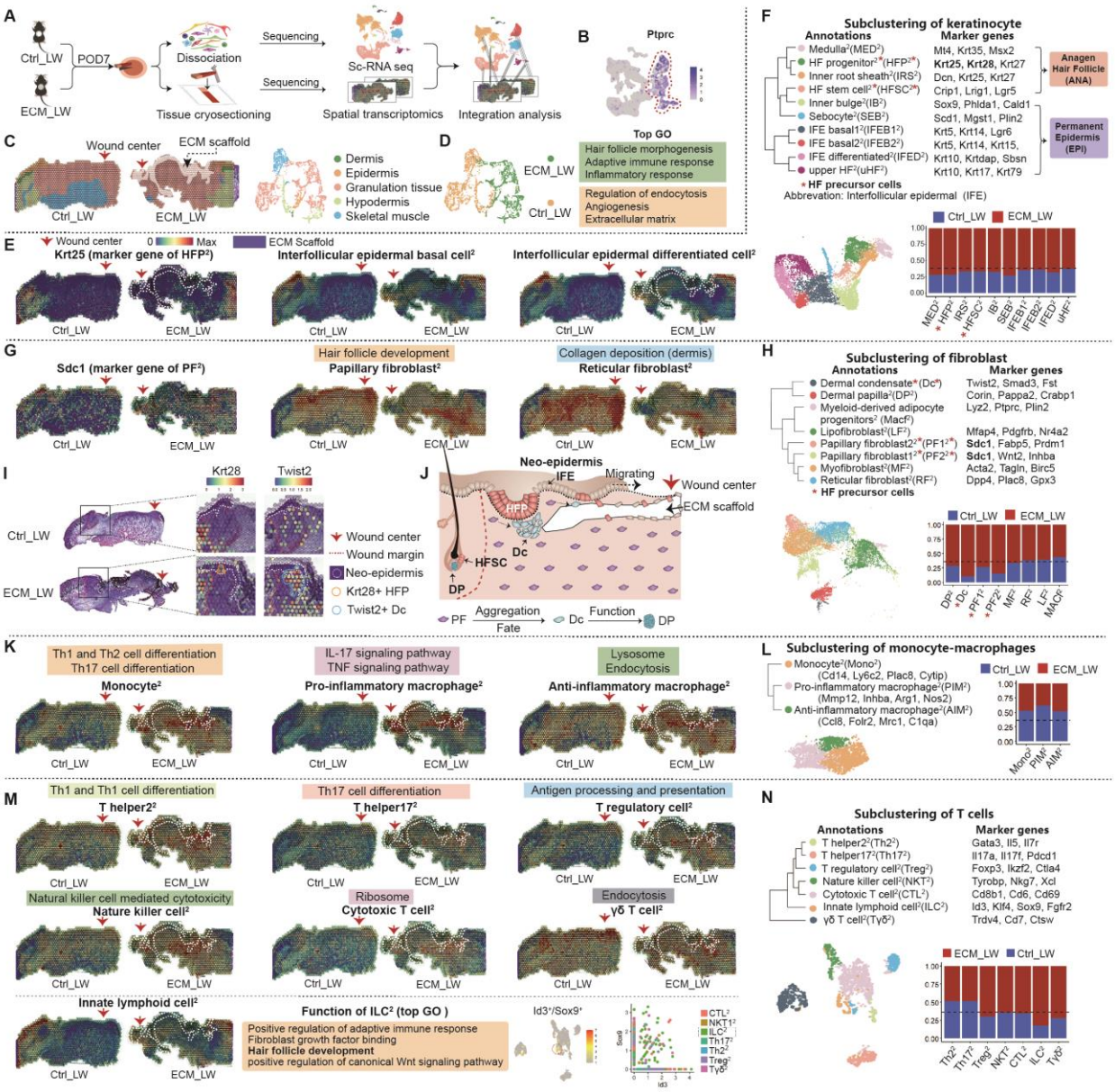

Fig. 4. Spatial transcriptomics applied to ECM_LW and Ctrl_LW. (A) Schematic for generating scRNA-seq and spatial transcriptomics data from splinted excisional wounds. (B) Feature plot showed the expression of Ptprc (Cd45) in scRNA-seq dataset. (C) The unsupervised clustering indicated the anatomical structure of sample. (D) Gene enrichment analysis between ECM_LW and Ctrl_LW. (E) Spatial feature plot showed the expression of Krt25 (marker gene for hair follicle progenitor) and defined keratinocyte subclusters in tissue sections. (F) Subclustering of keratinocyte in sc-RNA seq dataset. (G) Spatial feature plot showed the expression of Sdc1 (marker gene for papillary fibroblast) and defined fibroblast subclusters in tissue sections. (H) Subclustering of fibroblast in sc-RNA seq dataset. (I) Spatial feature plot

highlighted the expression of Krt28+ Hair follicle progenitor and Twist2+ Dermal condensate in migrating neo-epidermis. (J) Illustration showed the epithelialization along with de novo HF formation in ECM_LW group. (K) Spatial feature plot showed the expression of defined monocyte, macrophage (MAC) subclusters in tissue sections. (L) Subclustering of MAC in sc-RNA seq dataset. (M) Spatial feature plot showed the expression of defined T cell subclusters in tissue sections. (N) Subclustering of T cell in sc-RNA seq dataset.

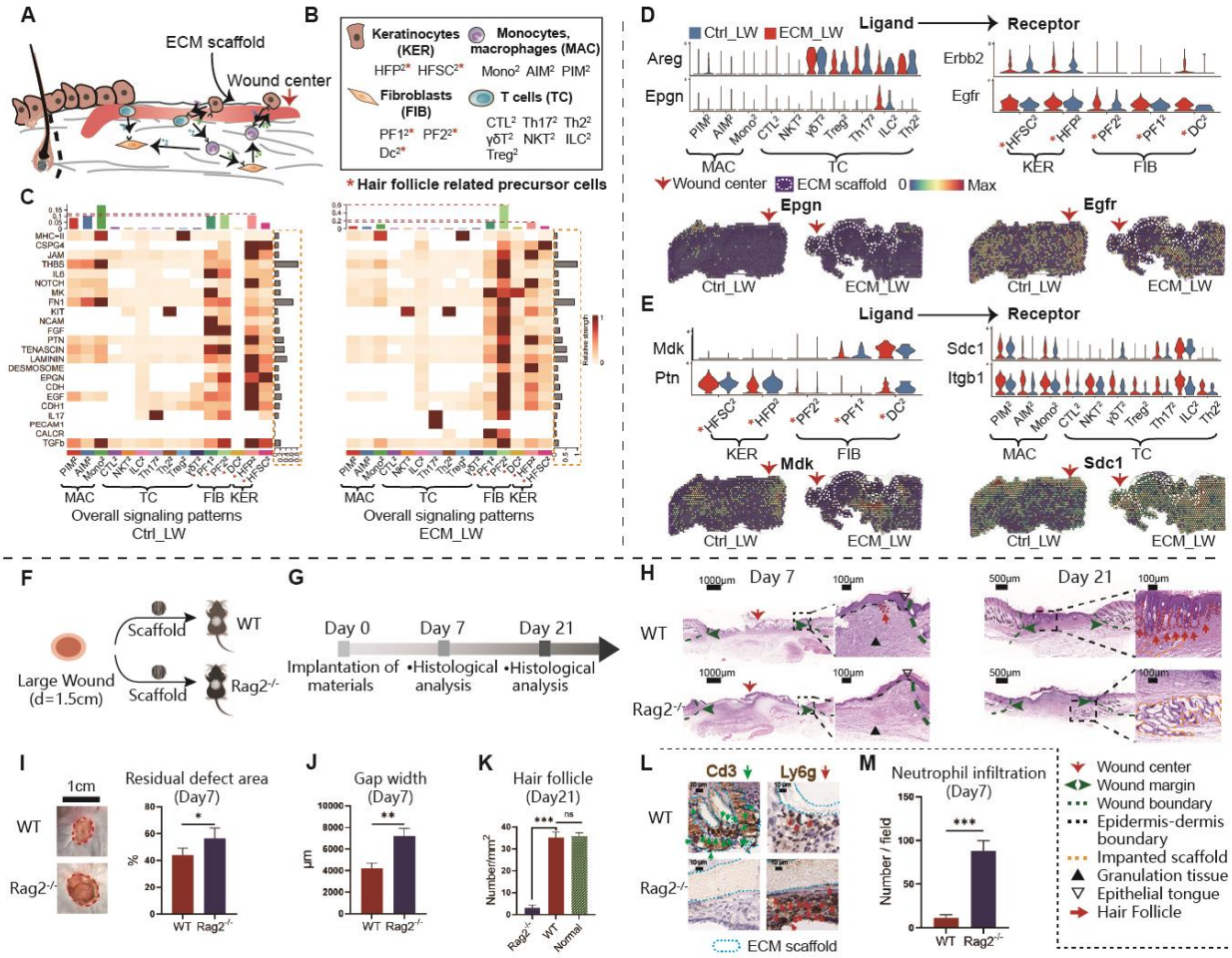

Fig. 5. Cellular communication landscape between immune cells and cutaneous cells in ECM_LW and Ctrl_LW group. (A) Schematic of combined ligand-receptor analysis between cutaneous cells and adaptive immune cells . (B) Defined subclusters in corresponding scRNA-seq dataset. (C) Comparison of overall cell-cell communication patterns between Ctrl_LW and ECM_LW using CellChat. (D and E) Violin plot (scRNA-seq) and spatial feature plots (ST) showed select ligands and cognate receptor expression. (F) Surgical process and (G) workflow for evaluating large area wound healing mediated by ECM scaffold in Rag2$^{-/-}$ and WT mice. (H) Residual defect area at 7 days after wound. (I) Histological analysis of wound healing in WT and Rag2$^{-/-}$ mice. (J) Semiquantitative evaluation of gap width. (K) Histologic quantification of de novo HFs. (L) IHC staining of Cd3 and Ly6g. (M) Quantification of Ly6g^{+} neutrophil infiltration.

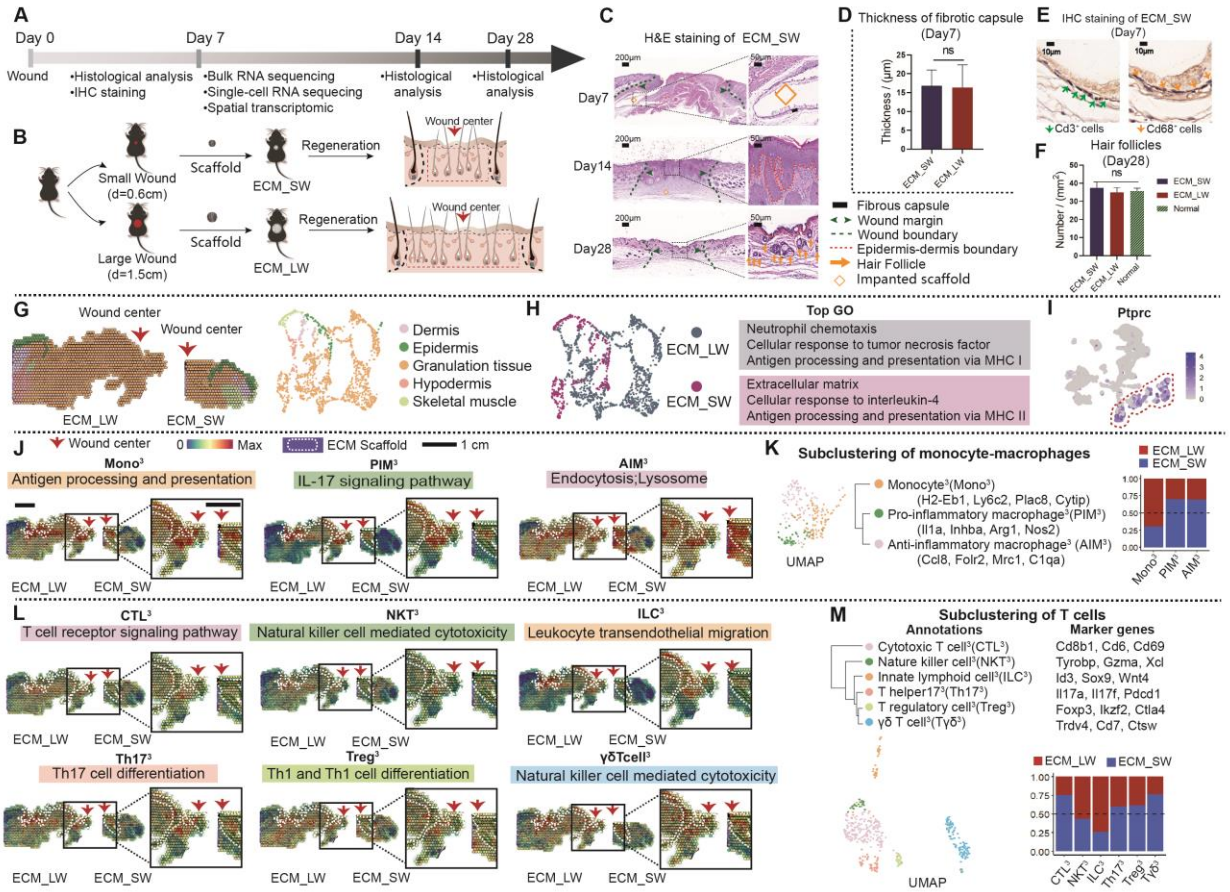

Fig. 6. Evaluation of the healing of small and large full-thickness wound with implanted ECM scaffolds. (A) Workflow for evaluating skin wound healing. (B) Surgical process for skin excisional wound model of ECM_SW and ECM_LW group. (C) H&E staining of ECM_SW samples. (D) Thickness of fibrotic capsule around membrane of ECM_SW and ECM_LW group. (E) IHC staining of Cd3 and Cd68. (F) Histologic quantification of de novo hair follicles on POD28. (G) The unsupervised clustering indicated the anatomical structure of sample. (H) Gene enrichment analysis between ECM_LW and ECM_SW. (I) Feature plot showed the expression of Ptprc (Cd45) in scRNA-seq dataset. (J) Spatial feature plot showed the expression of defined monocyte, macrophage (MAC) subclusters (related to fig.S12) in tissue sections. (K) Subclustering of MAC in sc-RNA seq dataset. (L) Spatial feature plot showed the expression of defined T cell subclusters (related to fig.S12) in tissue sections. (M) Subclustering of T cell in sc-RNA seq dataset.

Supplementary Materials for

Tracing immune cell around biomaterials with spatial anchor during wound regeneration

Yang Yang1†, Chen-yu Chu1†, Yi Man1†, Li Liu1†, Chen-bing Wang1, Chen Hu1, Xin-hui Li1, Yi-li Qu1*

† These authors contributed equally to this work

Correspondence to: qqyili@126.com (Y.L.Q.)

This PDF file includes:

Materials and Methods
Supplementary Text
figs. S1 to S12
References (39–##)

Materials and Methods

Fabrication of ECM scaffolds

The preparation of ECM scaffolds was similar to our previous report(*1*).To fabricate the electrospinning scaffold with approximate 300nm diameter aligned fibers, 20% w/v PLGA (LA/GA = 75:25, molecular weight = 105 kDa, Jinan Daigang Biomaterial Co. Ltd.) and 2% w/v FC (Sangon Biotech Co. Ltd.) were dissolved in HFIP (Aladdin Co., Ltd.) with stirring until complete dissolution. The solution was fed at 0.018mm/min, and a voltage of -2/5kv and 11 cm distance between the needle (21G) and the rotating cylinder (2800 rpm) was applied. After been dried in a vacuum oven for a week, The morphology of PLGA/FC nanofibrous scaffold was observed by the scanning electron microscopy (SEM; JSM-7500F, JEOL, Japan). The scaffolds were cut into circular shape (0.8cm or 1.8cm in diameter) and sterilized using γ-irradiation before the animal implantation experiments.

Excisional wound model and implantation procedures

All procedures involving animals were approved by the Institution Review Board of West China Hospital of Stomatology (No. WCHSIRB-D-2017-033-R1). C57BL/6J mice (Dossy Experimental Animals Co., Ltd.) and immunodeficient C57Bl/6 (B6.129-Rag2tm1) mice (Shanghai Model Organisms Center Inc., Shanghai, China), at the age of 6 week (~20 g) were used in this research. The circular (diameter =0.6, 0.9, 1.2, 1.5cm) full-thickness wound were created in the mice dorsal skin. The mice in further study were divided into four groups: small wounds (diameter = 0.6cm) transplanted with saline (Ctrl_SW) or biosynthetic ECM scaffolds below the wound (ECM_SW), and large wound (diameter = 1.5cm) transplanted with saline (Ctrl_LW) or biosynthetic ECM scaffolds below the wound (ECM_LW). Subsequently, the wounds were covered with sterile Tegaderm film (3M) and respectively fixed on the small (inner diameter 8 mm and outer diameter 12 mm, for small wound) or large (inner diameter 18 mm and outer diameter 22 mm, for large wound) silicone ring with uniform suture. Mice were euthanatized at 1, 2, and 4 weeks after the surgery, and the small (diameter 10 mm, for small wound) or large (diameter 25 mm, for large wound) round full-thickness sample was harvested.

Bulk RNA sequencing

Three replicates of mice skin wounds in each group were collected for the of Bulk RNA sequencing procedure. Total amounts and integrity of RNA were assessed using the RNA Nano 6000 Assay Kit of the Bioanalyzer 2100 system (Agilent Technologies, CA, USA). mRNA was purified from total RNA by using poly-T oligo-attached magnetic beads. The library fragments were purified with AMPure XP system (Beckman Coulter, Beverly, USA). The PCR amplification product was purified by AMPure XP beads. After the library is qualified by qRT-PCR, the different libraries are pooling and being sequenced by the Illumina NovaSeq 6000. FeatureCounts (v1.5.0-p3) was used to count the reads numbers mapped to each gene. And then FPKM of each gene was calculated based on the length of the gene and reads count mapped to this gene. Differential expression analysis of two groups (three biological replicates per group) was performed using the DESeq2 R package (1.20.0), p−value <0.05 and $|\log_2(\text{foldchange})| > 1$ was set as the threshold for significantly differential expression. GO terms and KEGG pathways with corrected P-value less than 0.05 were considered significantly enriched by differential expressed genes.

Single cell RNA sequencing

Specimen harvest procedure for scRNA-seq was like our previous report(*2*),3~4 fresh samples were collected per group. In brief, the wound tissues were firstly digested by the Epidermis Dissociation Kit (Epidermis Dissociation Kit, mouse; Miltenyi Biotec) for enzymatic epidermal-dermal separation. The epidermis part was dissociated by a gentleMACS Dissociator (Miltenyi), then filtered (70-mm cell strainer, Corning, Durham), centrifuged (300g, 10 min, 4°C), and resuspended with phosphate-buffered saline (PBS) containing 0.5% bovine serum albumin (BSA). The dermis part was cut into 1 mm width pieces and mixed with mixed enzyme solution containing type I collagenase (Gibco, Grand Island) and trypsin (Gibco, Canada), then dissociated by gentleMACS Dissociator (Miltenyi), and digested for 2.5 hours in a hybridization oven (Peqlab PerfectBlot). After being dissociated, filtered, centrifuged, and resuspended in red blood cell lysis buffer (Solarbio), the dermis cells were mixed with epidermis part. Then the dead cells and debris were removed by Dead Cell Removal MicroBeads (Miltenyi). Lastly, these suspensions were then carried out for Single-Cell RNA-seq (10x Genomics Chromium Single Cell Kit). Sequencing (10x Genomics Chromium Single Cell 3′ v3) was performed using an Illumina 1.9 mode. Then, reads were aligned, and expression matrices were generated for downstream analysis (Cell Ranger pipeline software). Filtering, normalization, scaling and canonical correlation analysis were performed (Seurat 4.1.2.) for integrated datasets. CellChat was used to predict receptor-ligand probability among cell subpopulations.

Spatial Transcriptomics

Fresh samples were rapidly harvested and frozen in OCT. Wound tissues were cryosectioned at -20 degrees onto gene expression slides. Tissue sections on the Capture Areas of the Visium Spatial Gene Expression are fixed using methanol, H&E staining images will be used downstream to map the gene expression patterns. Using the Visium Tissue Optimization Slide & Reagent kit, permeabilization time was optimized. Second Strand Mix is added to the tissue sections to initiate second strand synthesis. After transfer of cDNA from the slide, spatially barcoded, full-length cDNA is amplified via PCR to generate sufficient mass for library construction. The final libraries contain the P5 and P7 primers used in Illumina amplification. A Visium Spatial Gene Expression library comprises standard Illumina paired-end constructs which begin and end with P5 and P7.Raw FASTQ files and histology images were processed (SpaceRanger software) for genome alignment. Raw output files for each group were read into R studio (Seurat 4.1.2). Normalization across spots was performed with the SCTransform function. The spatial cluster gene signature overlap correlation matrix was generated by first taking all genes differentially expressed (avg_log2FC > 1 and adjusted p value < 0.05) across all ST clusters. Pearson correlation was calculated across this matrix and hierarchical clustering of ST clusters was performed with the heatmap function with the ggplots package. Signature scoring derived from scRNA-seq and ST signatures was performed with the AddModuleScore function.

Histopathology, Immunohistochemistry, and immunofluorescence microscopy

The samples were fixed with 4% paraformaldehyde at least 48 hours before ethanol and xylene dehydration. H&E staining and Masson's trichrome staining were performed for the observation of re-epithelialization and collagen fiber deposition. Immunofluorescence staining for cytokeratin 5 (ab52635, Abcam, 1:200) and cytokeratin 10 (ab76318, Abcam, 1:150) and was performed for to assess keratinization. For the evaluation the infiltration of immune cells, immunohistochemistry staining for Cd3 (14-0032-82, Thermo Fisher Scientific, 1:100), Cd68 (ab283654, Abcam, 1:100), Ly6g (ab238132, Abcam, 1:2000) and immunofluorescent staining for Cd3 (14-0032-82, Thermo Fisher Scientific, 1:100), Cd68 (ab201844, Abcam, 1:250) were performed.

Flow cytometry analysis

The surface markers of T cells (CD3), monocyte, and macrophages (CD11b, CD68) were examined using flow cytometry to quantification the infiltration of immune cells. The digested cell solutions were coincubated with antibodies against CD68 (Allophycocyanin, ab221251, Abcam), CD3 (fluorescein isothiocyanate, catalog no. 100203, BioLegend), and CD11b (PerCP/Cy5.5, catalog no. ab210299, Abcam) at 1:400 dilution for 30~60 min at 4°C in the dark (100 μl per antibody per sample). Before the staining of CD3, cells were preincubated with purified anti-CD16/CD32 antibody (catalog no. 101301, BioLegend) (1.0 μg per 10^6 cells in 100 μl volume) for 5 to 10 min to block Fc receptors. Flow cytometry analysis was performed using Attune Nxt flow cytometer (Thermo Fisher Scientific) and FlowJo 10.8.1. The experiments were performed three times independently (n = 3).

Statistics and reproducibility

At least three independent replicates were conducted to obtain repeatable data, and the data was dealt with Case Viewer software, Image J software, and Prism 8.0 software. Statistical analyses were performed by Student's t-test or one-way analysis of variance (ANOVA) with Tukey post-hoc test. The numerical data are presented as mean ± standard deviation. A value of $p < 0.05$ was considered statistically significant (*$p < 0.05$, **$p < 0.01$, ***$p < 0.001$), and ns means no statistically significant difference.

Supplementary Text

Cell type annotation of scRNA-seq data

Ctrl_LW VS Ctrl_SW

Firstly, we undertook scRNA-seq to compare the transcriptional profiling between Ctrl_SW and Ctrl_LW group at single-cell resolution (fig. S1A). After quality control, 18,621 cell were included in the final dataset (11,217 from the Ctrl_LW group and 7,404 from the Ctrl_SW group). We firstly categorized the cells into 10 main clusters based on gene expression profiles using Seurat, and the proportion of cells from two groups were shown in fig. S1B. Top (based on average |log2FC| value) marker genes for each cell cluster were shown in the fig. S1C.

<u>*Subclustering of fibroblast*</u>

Firstly, we extracted cells defined as fibroblast and performed subcluster analysis (fig. S2A) based on marker genes profiles published before(*2-9*) (fig. S2B).Since dermal papilla (DP) cells ($Papp2^+Corin^+$) belonged to the existing HF in normal skin adjacent to the wound, which was not the focus of this part. We next conducted in-depth analysis of wound fibroblasts and defined them as following categories: upper layer papillary fibroblast (PF) ($Crabp1^+Fabp5^+$), lower layer fibroblast including reticular fibroblasts (RF) ($Dpp4^+Mgp^+Gpx3^+Plac8^+$) & hypodermis lipo-fibroblast (LF) ($Mfap4^+$ $Cd34^+$), as well as wound-activated myofibroblast ($Acta2^+Tagln^+Mki67^+$) and myeloid-derived adipocyte progenitors (Macf) ($Pdgfra^+$ $Lyz2^+$ $Ptprc^+$ $Plin2^+$). The heterogeneity of fibroblast subclusters might explain the reason why small wound generally heal with scarring devoid of HFs. In accordance with previous report(*3*), the major initial wave of dermal repair in small wound is mediated by the lower lineage fibroblast including LF (49.88%) and RF (21.93%) (fig. S2C), which is respectively related to hypodermis adipocytes formation and dermis collagen fibril organization (fig. S2D).The predominance of RF and LF in small wound might be the main cause for the excessive collagen deposition(*10*). In contrast, there were more upper lineage PF (36.11%) in large wound (fig. 2C). The PF in this dataset consisted of 2 subclusters including PF1 ($Runx1^+Inhba^+$)(*4*) and

PF2 (Notch1^{+}Prdm1^{+})(*11*), both of which were believed to have the capacity to support HF initiation (fig. S2D). Intriguingly, there were 134 Macf cells specifically exist in large wound, which had been proved to be the progenitors of adipocyte around neo-HF in large wound center(*6*).

Subclustering of keratinocyte

Next, we extracted cells assigned as keratinocyte and performed subcluster analysis. Known markers(*2, 8, 12-14*) were used to define keratinocyte subclusters identity (fig. S2 E-G). Hair follicle stem cell (HFSC) (Lgr5^{+}Lrig1^{+})(*14*) and HFP (hair follicle progenitor) (Msx2^{+}Krt28^{+}Mki67^{+})(*13*) were believed to be the dominant epithelial contributor to the de novo HF. The proportion of HFP was higher in Ctrl_LW (12.97%) than Ctrl_SW (3.14%). Collectively, the higher proportion of HF precursor cells including PF (mesenchymal origin), HFSC and HFP (epithelial origin) may account for the initiation of WIHN specially in large wound. Besides, since the HF cycles through phases of growth (anagen), regression (catagen), and rest (telogen)(*8*). Keratinocytes could be robustly assigned to two cell types: permanent part of the epidermis (interfollicular epidermis, sebaceous gland, and non-cycling portion of the HF) and keratinocytes from the cycling part of the anagen HF. The anagen HF cells in this dataset were composed of (Ube2c^{+}Ccnb1^{+}) germinative layer (GL) cells, (Mt4^{+} Rnaset2b^{+}Krt35^{+}) medulla (MED) and cortex cells, and (Krt25^{+}Krt27^{+}) inner root sheath (IRS) layers cells. Since the C57/B6 mice were in their second telogen (postnatal days P46–70) on POD7.The higher proportion of anagen HF cells in Ctrl_LW suggested a stronger HF telogen–anagen transition (TAT) around the large wound as well.

Subclustering of monocyte and macrophages

Macrophages are highly plastic immune cells upon different environment stimulators and contribute to most phases of tissue repair(*15*).They phagocytose pathogens or debris instantly in response to wounding. Then, they activate the adaptive immune system through specific antigen presentation, which is believed to bridge the innate and adaptive immune system(*16*).To explore the heterogeneity of macrophages, we extracted the monocyte and macrophages (MAC) and subjected them to further subcluster analysis. Canonical classification systems of macrophages including “classically activated” M1 macrophages and “alternatively activated” M2 macrophages were shown insufficiently to identify the phenotypes in this condition (fig. 3B).Based on known markers(*2*), three subsets including Ccl8^{+} Folr2^{+}C1qa^{+}Mrc1^{+} anti-inflammatory macrophages (AIM), Mmp12^{+}Arg1^{+}Inhba^{+}Nos2^{+} pro-inflammatory macrophages (PIM) and Ly6c2^{+}Plac8^{+}Cytip^{+}H2-Eb1^{+} monocyte (Mono) were determined (fig. S3 A-C). The pseudo-temporal trajectory of the three subsets revealed that monocytes developed into PIM firstly and then polarized into AIM (fig. S3E). KEGG enrichment analysis revealed that Mono might play role in antigen presentation and T cell differentiation, and Mono in Ctrl_LW group specifically related to nature killer cell mediated cytotoxicity; PIM was related to pro-inflammatory pathways, among which IL-17 pathway was up-regulated in Ctrl_LW group; AIM was correlated to lysosome, phagosome, and endocytosis which belonged to innate immune response (fig. S3D).The higher proportion of all three macrophage subsets as well as neutrophil and dendritic cell in Ctrl_LW (fig. S4) suggested there was a more complex environment both in innate immune response as well as the activation of adaptive system in large wound.

Subclustering of T cells

Recently, the role of adaptive immune cells on the formation of the pro-regenerative immune microenvironment has been stressed out(*17*). Although the role of γδ T cells in facilitating WIHN (*18, 19*) has been demonstrated, the

relationship of adaptive immune cells with HF regeneration is largely unknown till now. The proportion of T cell was higher in Ctrl_LW group (fig. S2B) in accordance with the result of bulk-seq and histological results. Based on published marker(*2, 20*), T cells were clustered into seven subsets (fig. S3 F-G) including Cd8b1^{+} cytotoxic T cell (CTL), Tyrobp^{+}Nkg7^{+}Xcl^{+} nature killer T cell1 (NKT1), Tyrobp^{+}Ccl2^{+} nature killer T cell2 (NKT2), Il17f^{+} T helper17 (Th17), Foxp3^{+} T regulatory cell (Treg), Trdv4^{+}Cd7^{+}Ctsw^{+} γδT cell1 (Tγδ1) and Cd7^{+}Ctsw^{+}Gnb21l^{+} γδT cell2 (Tγδ2). As shown in fig. S3F, γδT cell was the only predominant subtype of T cell in Ctrl_SW (70.82%), which was related to endocytosis belonging to innate immune system (fig. S3H). In contrast, there were more abundant subtypes of adaptive αβT cells in Ctrl_LW group, which were related to Th17 and Th1/Th2 cell differentiation. Besides, the proportion of Ccl2^{high} NKT2 cell was also higher in Ctrl_LW, which was related to the recruitment of inflammatory macrophage(*21*). What's more, there were more Tregs in large wound which were believed to paly role in suppressing excessive collagen deposition and driving HFSC differentiation &migration(*22*). To sum up, the diverse subtypes of T cell from Ctrl_LW group suggested a more active adaptive immune micro-environment in skin large wound.

ECM_LW vs Ctrl_LW

To explore how ECM scaffold regulated the microenvironment in large wound, we isolated cells from the ECM_LW and Ctrl_LW samples and applied them to the 10x scRNA-seq platform (fig. S8A). After cell filtering, 31,740 single-cell transcriptomes were included in the final dataset (20,312 for the ECM_LW group and 11,428 for the Ctrl_LW group). Unsupervised clustering using Seurat categorized the cells into 10 main classes of cells. The composition of each cell cluster was listed so that the proportion of cells from two groups could be identified across all cell clusters (fig. S8B). Marker genes for each cell cluster were shown in the heatmap in fig. S8C. Genes related to T cells (Il7r, Areg and Tubb5) were substantially higher expressed by the ECM_LW (fig. S8D).

Subclustering of fibroblast

Firstly, As shown in fig. S9A, we defined most fibroblast subclusters based on defined markers in fig. S9B. Remarkably, we identified the Smad3^{+}Lef1^{+}Krt17^{+} dermal condensate (Dc) cell(*23*) specially in this dataset. Derived from PF, The Dc was believed to be the origin of DP reside at the base of the adult HF (*23, 24*).Since approximate 90% of Dc were from ECM_LW group, as well as significantly higher proportion of PF1^{2} and PF2^{2} from ECM_LW (fig. S9C), which might provide enough mesenchymal component for the subsequent HF formation in ECM_implanted group (fig. S9D). In embryologic HF morphology, Dc is believed to be the signaling niches for epithelial HFP to form epithelial placode (Pc)(*23*), and thus promote HF growth.

Subclustering of keratinocyte

Based on known marker, we also find the higher proportion of HFP^{2} and HFSC^{2} in ECM_LW group (fig. S9 E-F), which might serve enough epithelial resources for nascent HF growth. What's more, the higher proportion of interfollicular epidermal basal cell^{2} (IFEB^{2}) and interfollicular epidermal differentiated cell^{2} (IFED^{2}) were observed in the ECM_LW group, supporting more neo-epithelium proliferation in the presence of scaffolds.

Subclustering of monocyte and macrophage

Macrophages were of vital importance in orchestrating biomaterial related FBR and tissue regeneration(*25*). Three subsets of macrophages including (Ccl8^{+}Folr2^{+}C1qa^{+}Mrc1^{+}) AIM^{2}, (Mmp12^{+}Arg1^{+}Inhba^{+}Nos2^{+}) PIM^{2} and (Ly6c2^{+}Plac8^{+}Cytip^{+}H2-Eb1^{+}) Mono^{2} were determined. The Ctrl_LW group contributed to a larger proportion of all

three subsets, suggesting that the scaffold might play a role in the reduction of macrophage infiltration at the proliferative stage (fig. S10 A~C).

Subclustering of T cell

T cells were the only immune cell which owned a higher proportion in ECM_LW group (fig. S8 B). Subclustering of T cells resulted in seven subsets (fig. S10 D-H). In addition to $Cd8b1^{+}$ cytotoxic T $cell^{2}$ (CTL^{2}), ($Tyrobp^{+}Nkg7^{+}Xcl^{+}$) nature killer $cell^{2}$ (NKT^{2}), ($Il17a+Il17f^{+}$) T $helper17^{2}$ ($Th17^{2}$), $Foxp3^{+}$ T regulatory $cell^{2}$ ($Treg^{2}$), and ($Trdv4^{+}Cd7^{+}Ctsw^{+}$) γδT $cell^{2}$ ($T\gamma\delta^{2}$) which had been defined in fig. S3 G, two new immune cell subclusters including ($Bcl11a^{+}Id3^{+}Notch1^{+}$) innate lymphoid cell (ILC) and ($Gata3^{+}Il5^{+}$) T helper2 (Th2) cell were identified in our dataset based on published research(*26, 27*). Derived from common lymphoid progenitors, ILCs mirror αβ T cell subtypes functionality responding to local signals but lack antigen-specific receptors. In skin, tissue resident ILCs play key roles in barrier integrity, inflammatory response initiation, and immunological response modulation in wound repairing(*27-30*). Correlation analysis showed that ILC and Th2 were respectively highly correlated with CTL^{2} and $Th17^{2}$ (fig. S10 E). Remarkablely, skin-resident ILC in our dataset possessed a tissue specific transcriptional profile that co-expression genes related to T cell functionality ($Cd3d^{+}Klf4^{+}Fst^{+}Itga6^{+}$) and HF morphology ($Wnt4^{+}Sox9^{+}Fgfr2^{+}$). Gene enrichment analysis showed the ILC was related to bacterial invasion of epithelial, leukocyte transendothelial migration as well as hair follicle development (fig. S10 G-H). It was suggested that ILCs might initiate HF neogenesis by balancing reparative and pro-inflammatory function(*31*). Collectively, our dataset suggested that ECM-scaffold exerted the immune-regulatory effect on the further activation of adaptive systems in large wound healing, which might play role in HF development.

Subclustering of neutrophil

Firstly, activated by platelets, neutrophils are the first responding immune cells acting as the critical mediators of innate immune system. They are necessary for the degradation of biomaterials as well as recruitment and differentiation of monocytes(*32*). Four neutrophil subsets including $Il1b^{+}Retnlg^{+}$ peripheral blood neutrophil (PBN^{2}), $Il1a^{+}Tnf^{+}$ neutrophil1 (Neu1), $Lrg1^{+}Il1r2^{+}$ neutrophil2 (Neu2), $Ccl9^{+}Rgs1^{+}$ neutrophil3 (Neu3) were identified in our dataset (fig. S11 A-B). KEGG analysis showed the PBN^{2} was enriched in mitophagy, which was essential for neutrophil differentiation(*33*). Neu1 and Neu2 were respectively related to phagosome and Fc-gamma R mediated phagocytosis. While Neu3 showed gene enrichment in leukocyte migration and Th17 cell differentiation. Neu3 was the only subsets owned a higher proportion in ECM_LW group (fig. S11 C).

Subclustering of dendritic cell

Dendritic cell (DC) was classified into two subclusters including $Krt5^{+}Krt14^{+}$ langerhans cell (LC) and $Cd86^{+}$ monocyte derived dendritic cell (MDC) (fig. S11, D-E). KEGG analysis showed that LC and MDC respectively related to phagosome and antigen presentation (fig. S11 F). There was no obvious difference in the proportion of DC subsets between the two groups.

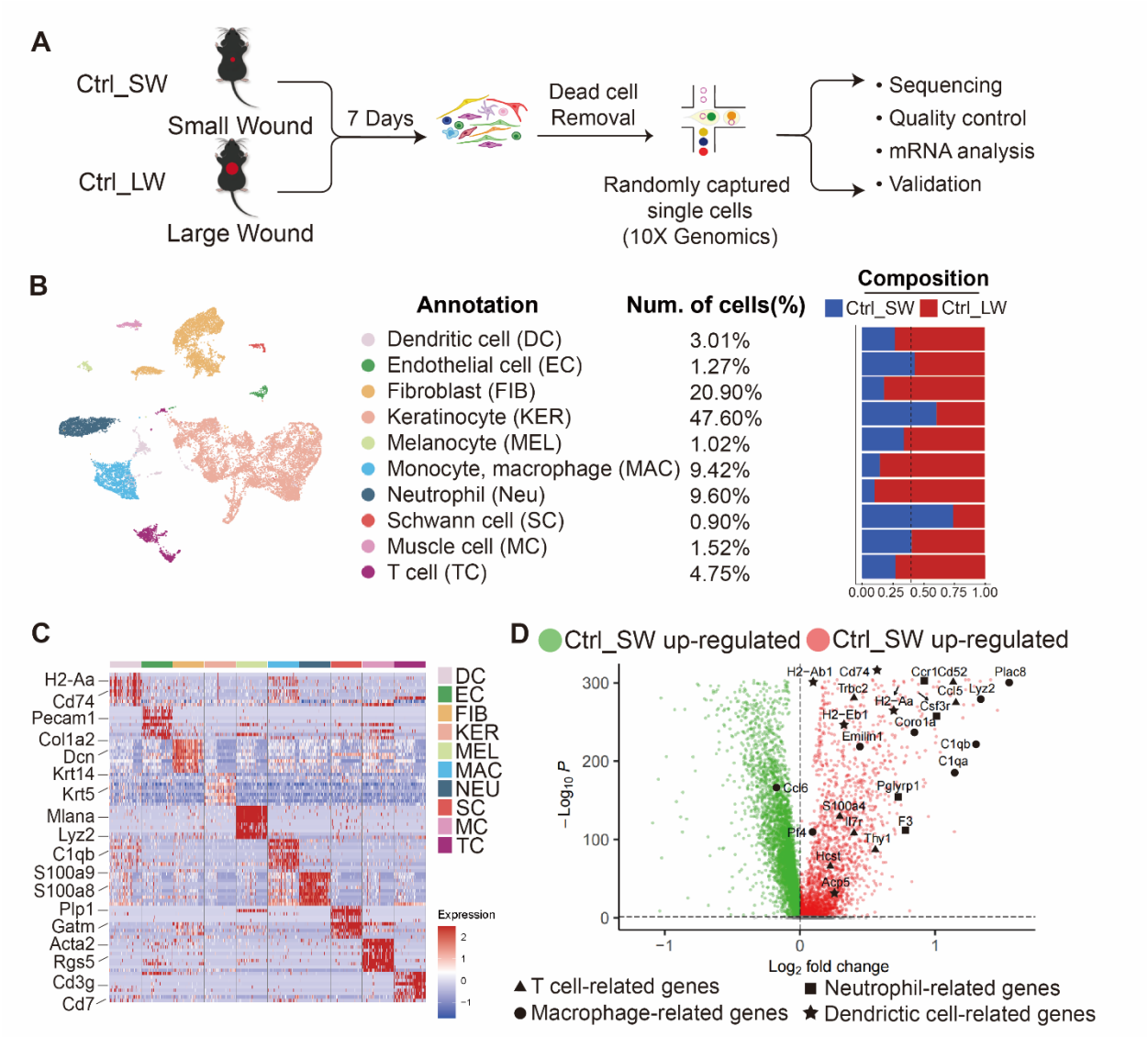

fig. S1. Overview of the single-cell transcriptome analysis between Ctrl_SW and Ctrl_LW. (A) Single-cell experiment workflow. (B) Cells were categorized into 10 main clusters. The number of cell populations in each cluster, number of cells (%), and composition of Ctrl_SW and Ctrl_LW groups were listed. (C) Heatmap showed top10 marker genes for different clusters. (D) Volcano plot showing interested differentially expressed genes in Ctrl_SW and Ctrl_LW group (scRNA-seq).

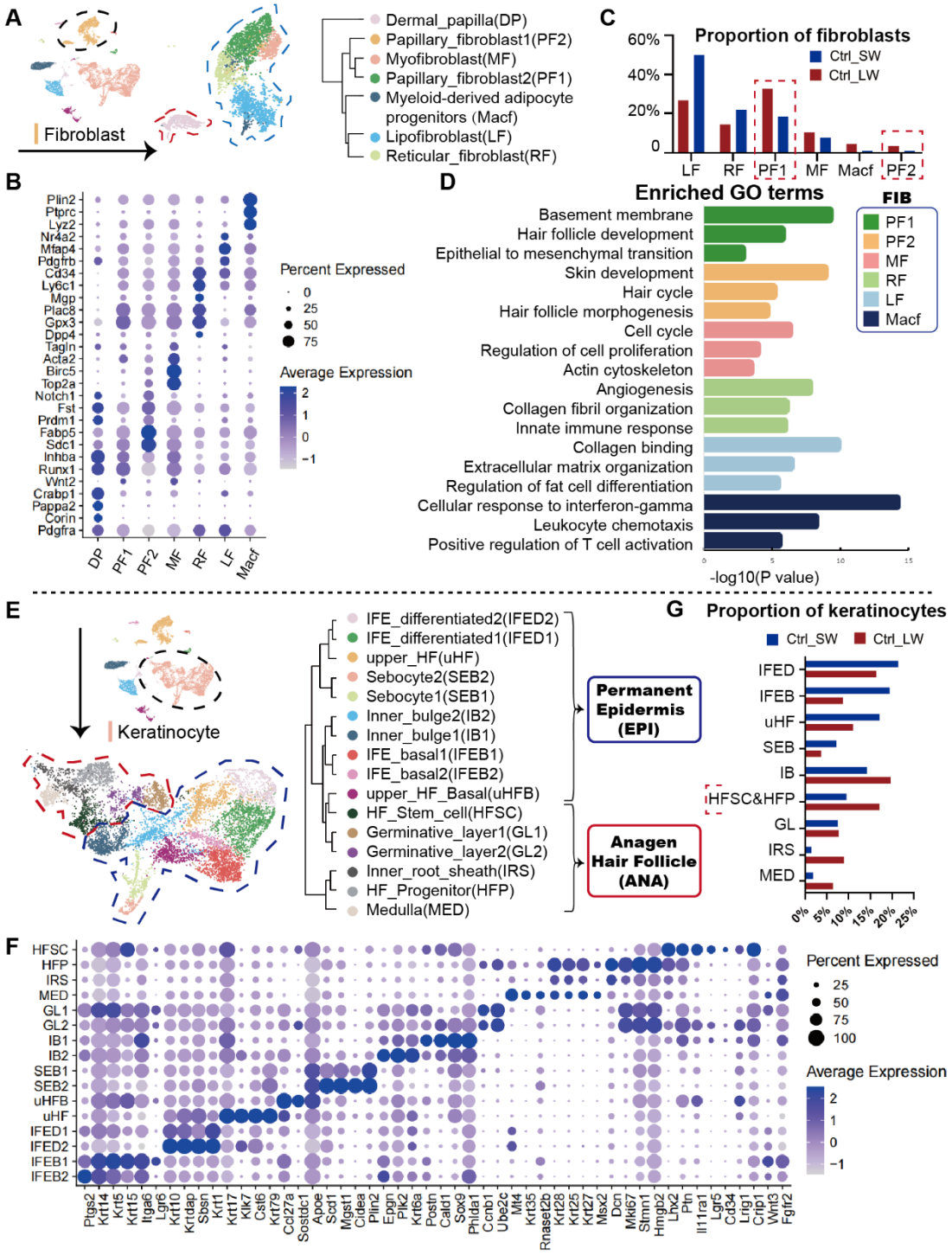

fig. S2. Further analysis of fibroblasts and keratinocytes between Ctrl_SW and Ctrl_LW. (A) Subclustering of fibroblasts showing 7 subsets and hierarchical clustering of average gene expression using pearson correlation analysis. (B) Marker genes for each fibroblasts subset. (C) Proportion of each subset in two groups. (D) GO enrichment analysis of wound fibroblast

subtypes. (E) Subclustering of keratinocytes showing 16 subsets and hierarchical clustering of average gene expression using pearson correlation analysis. (F) Marker genes for each keratinocytes subset. (G) Proportion of each keratinocytes subset in two groups.

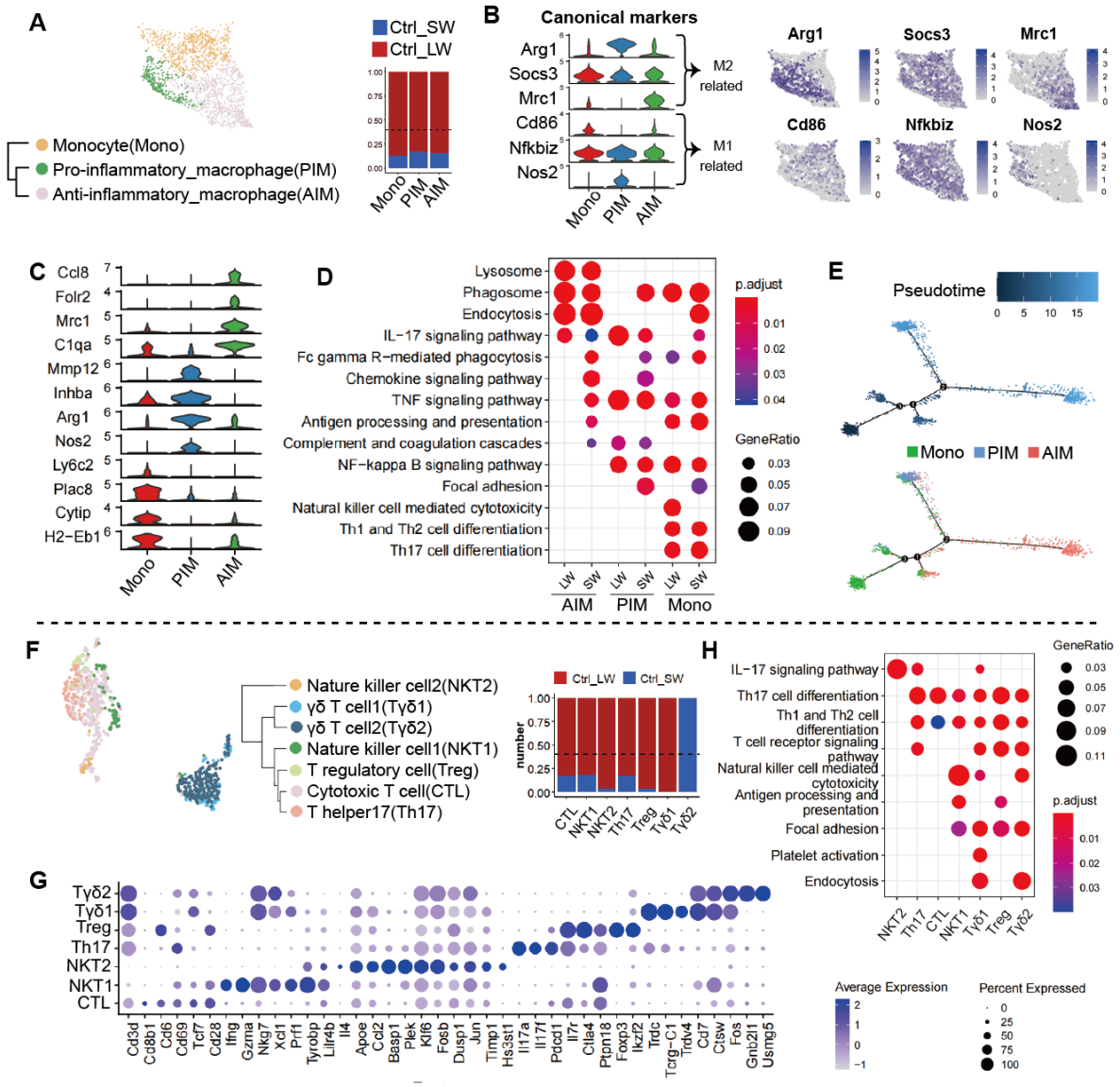

fig. S3. Analysis of MAC and T cells between Ctrl_SW and Ctrl_LW. (A) Subclustering of MAC showing three subsets and hierarchical clustering of average gene expression (pearson correlation analysis); The composition for each subset. (B) Expression of canonical M1 and M2 markers was inappropriate to identify the subtypes. (C) Marker genes for each MAC subset and (D) gene set enrichment analysis in KEGG pathway. (E) Pseudo-temporal ordering and the distribution of MAC subsets. (F) Subclustering of T cells showing seven subsets and hierarchical clustering of average gene expression (pearson correlation analysis); The composition for each subset. (G) Marker genes for T cell subsets and (H) gene set enrichment analysis in KEGG

pathway.expression using pearson correlation analysis. (F) Marker genes for each keratinocytes subset. (G) Proportion of each keratinocytes subset in two groups.

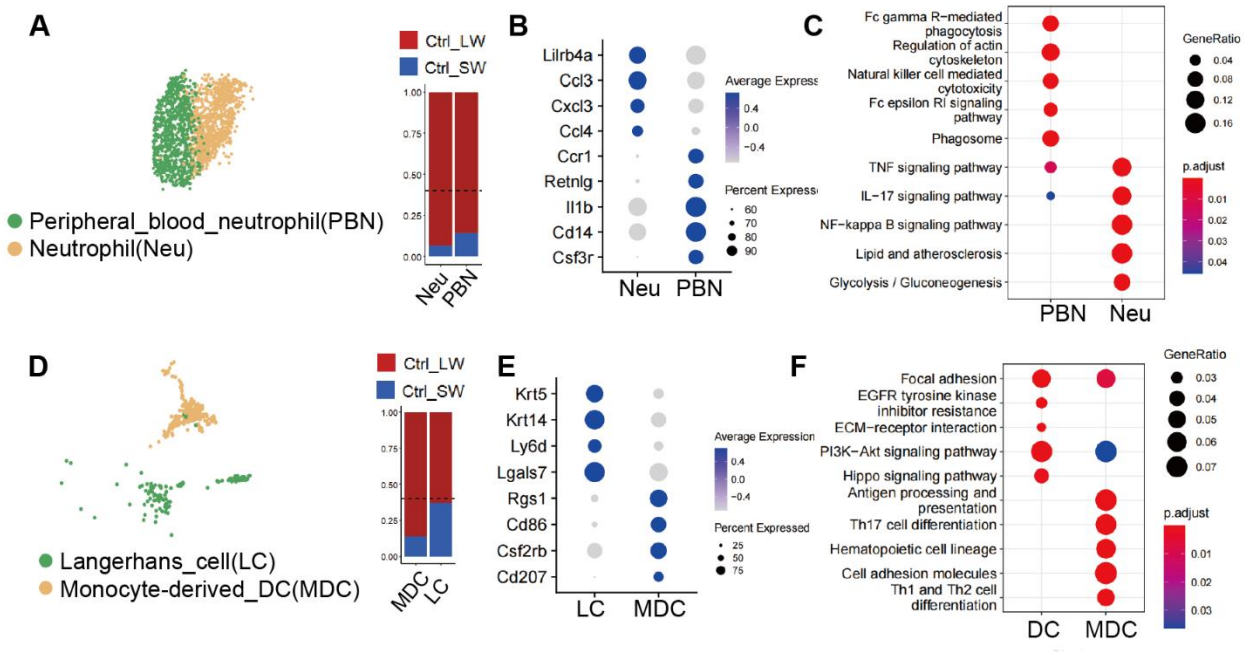

fig. S4. Further scRNA-seq analysis of neutrophils and dendritic cells between Ctrl_SW and Ctrl_LW. (A) Subclustering of neutrophils showing 2 subsets and the composition for each subset. (B) Marker genes for each neutrophil subset. (C) Gene enrichment analysis of KEGG pathway. (D) Subclustering of dendritic cells showing two subsets and the composition for each subset. (E) Marker genes for each dendritic cell subset. (F) Gene enrichment analysis of KEGG pathway.

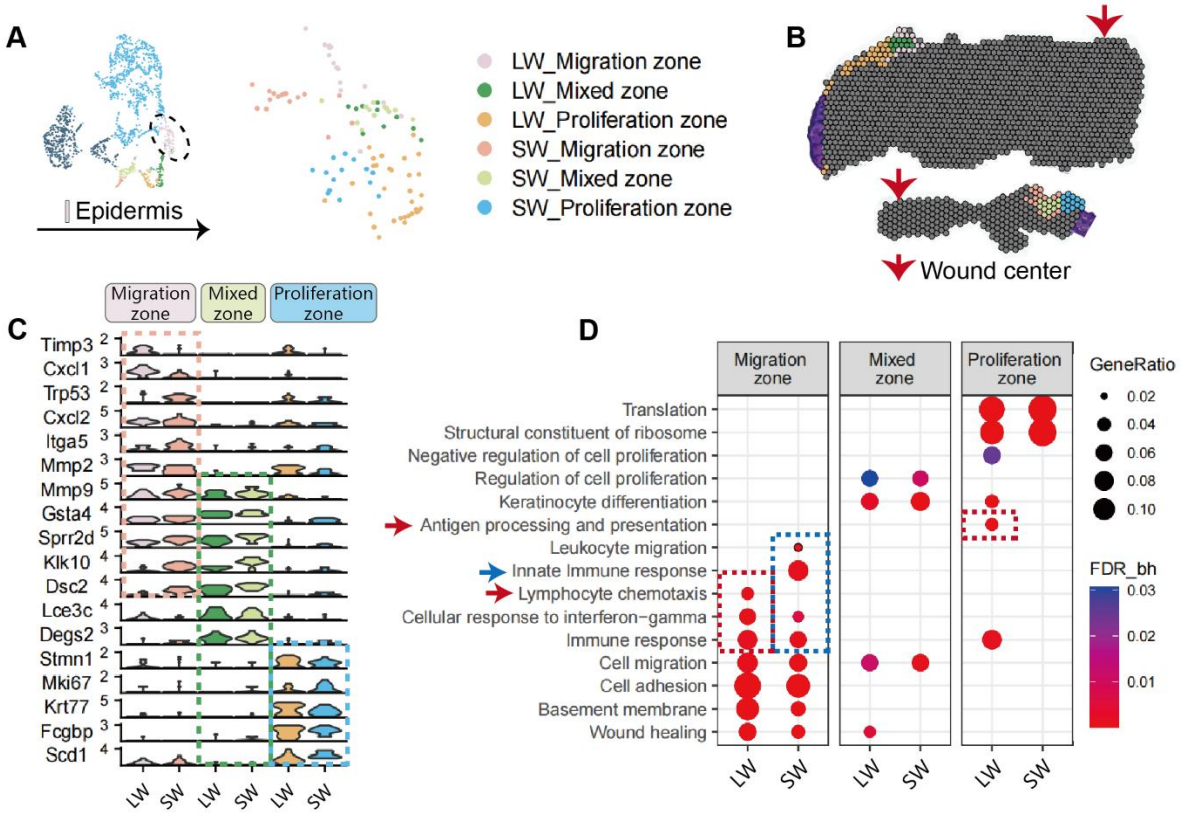

fig. S5. Further subclustering analysis of epidermis in Ctrl_SW and Ctrl_LW. (A)Subsets of epidermis in each group. (B) Corresponding spatial plot. (C) StackedVlnPlot showed marker genes differentially expressed in each region. (D) Enrichment analysis of GO terms.

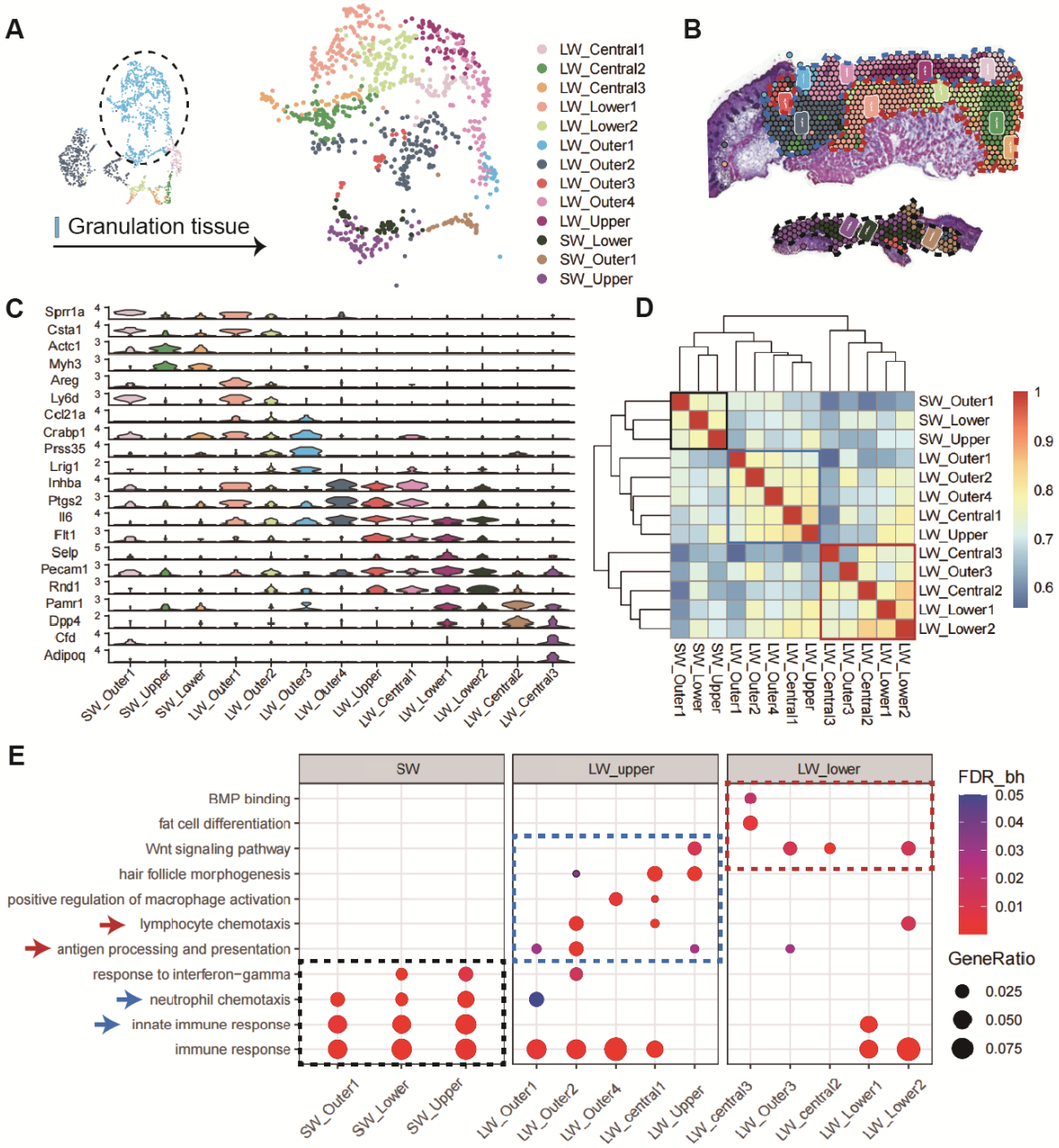

fig. S6. Further subclustering analysis of granulation tissue in Ctrl_SW and Ctrl_LW.

(A) Subsets of granulation tissue in each group. (B) Corresponding spatial plot of each region. (C) StackedVlnPlot showed marker genes differentially expressed in each region. (D) 13 regions were grouped into three functional clusters by pearson correlation analysis. (E) Enrichment analysis of GO terms.

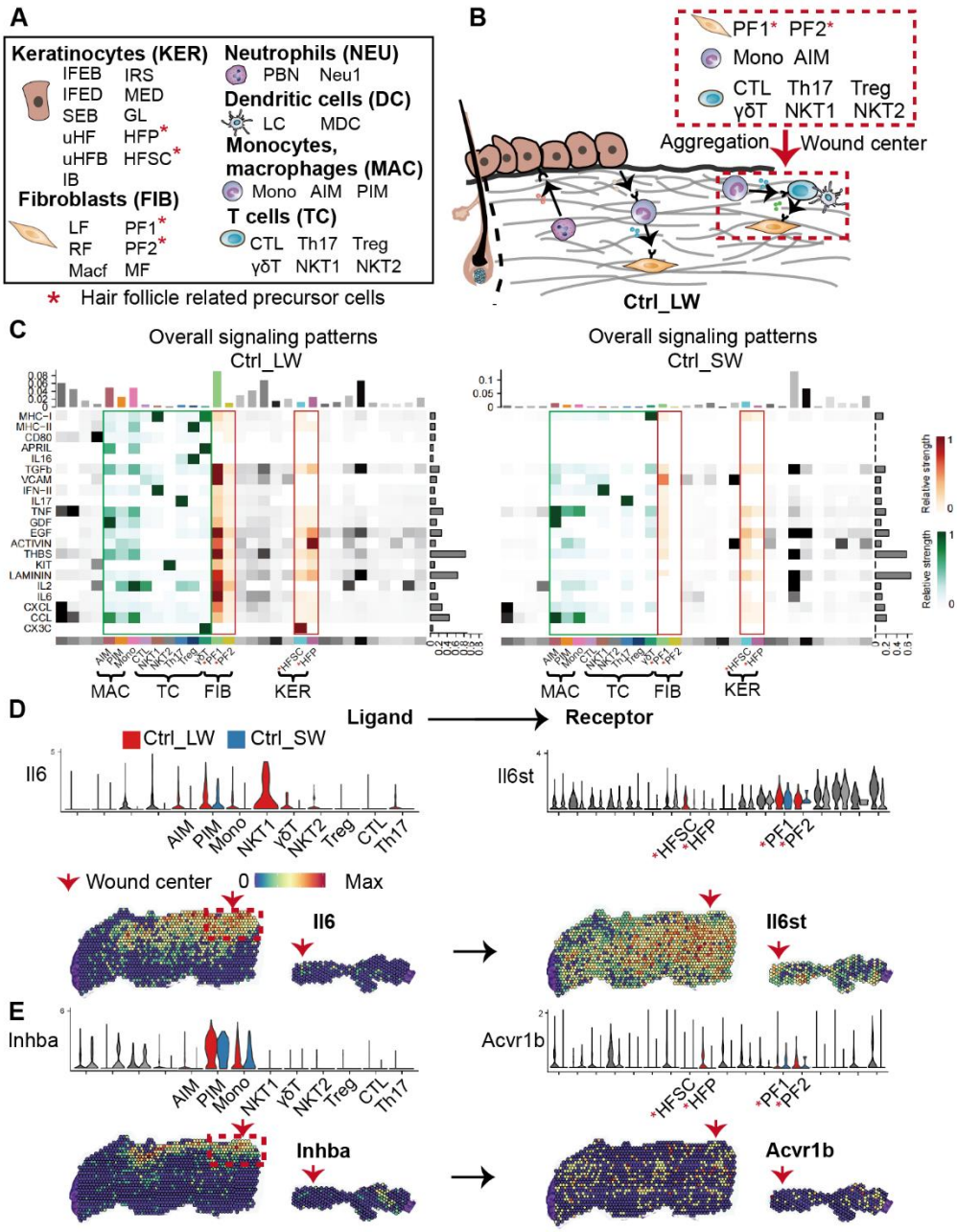

fig. S7. Cellular communication landscape between immune cells and cutaneous cells in Ctrl_SW and Ctrl_LW. (A) Defined subclusters in sc-RNA seq dataset (related to figure S2~S4) (B) Schematic of preferential aggregation of adaptive immune cells and papillary fibroblast in large wound center and combined ligand-receptor analysis between them. (C) Comparison of cell-cell communication patterns between Ctrl_SW and Ctrl_LW using CellChat. (D&E) Violin plot (sc RNA-seq) and spatial feature plots (ST) showed selected ligands expressed by immune cell subpopulations and cognate receptor expression by HF precursor cells.

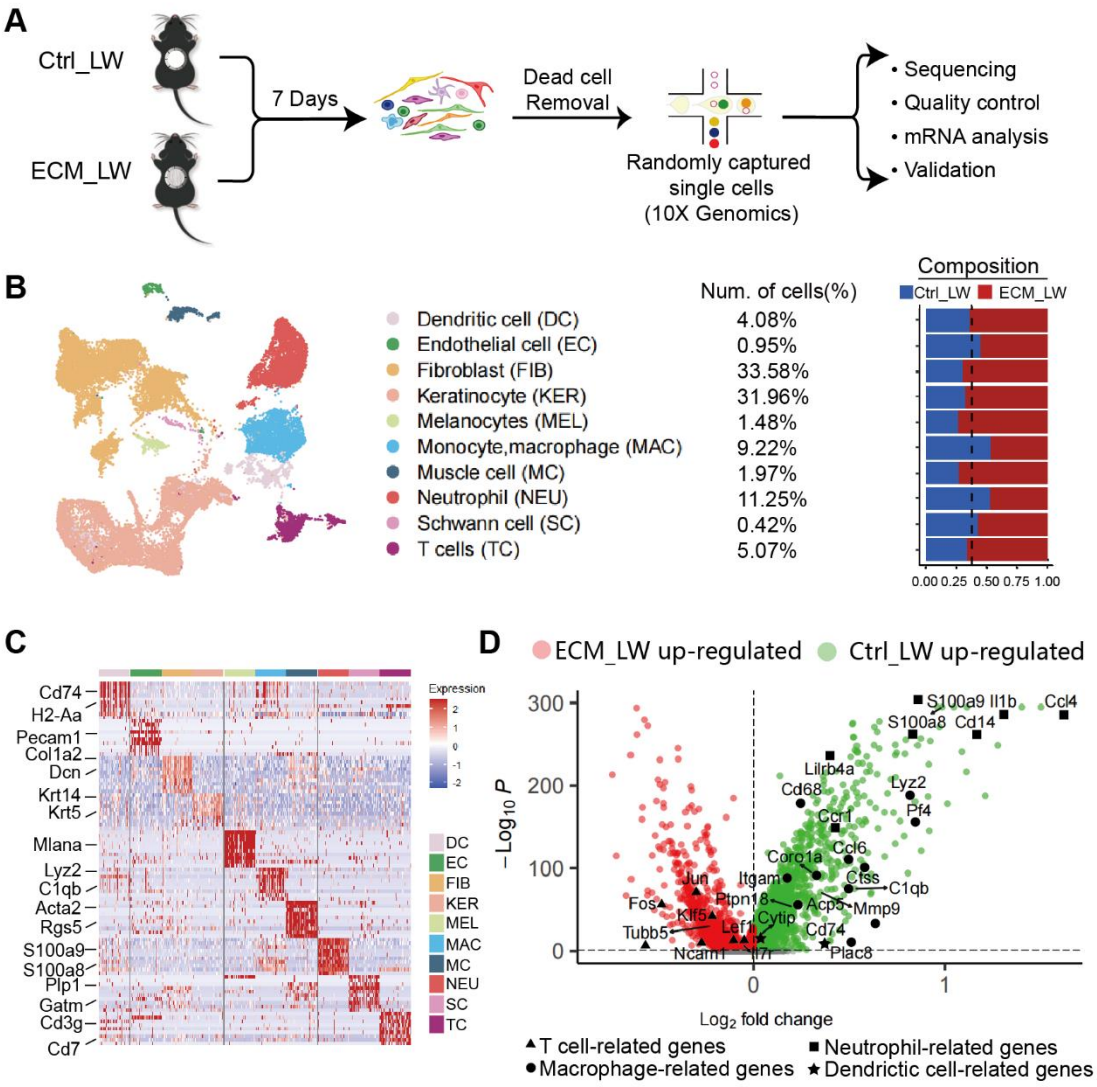

fig. S8. Overview of the single-cell transcriptome analysis between ECM_LW and Ctrl_LW. (A) Single-cell experiment workflow. (B) Cells were categorized into 10 main clusters. The number of cell populations in each cluster, number of cells (%), and composition of ECM_LW and Ctrl_LW groups were listed. (C) Heatmap showed top10 marker genes for each cluster. (D) Volcano plot showing interested differentially expressed genes in ECM_LW and Ctrl_LW group (scRNA-seq).

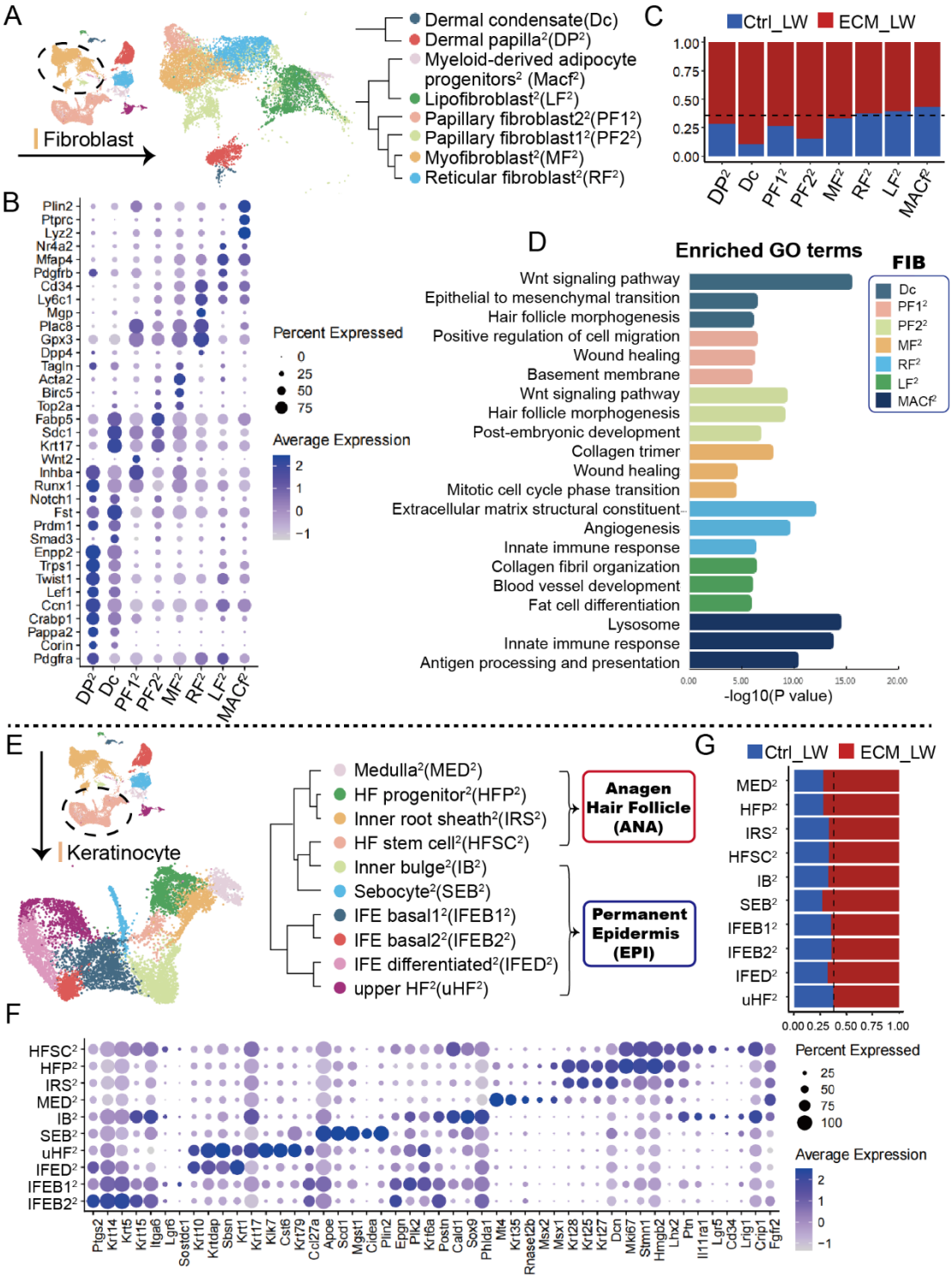

fig. S9. Further analysis of fibroblasts and keratinocytes between ECM_LW and Ctrl_LW. (A) Subclustering of fibroblasts showing 8 subsets; hierarchical clustering of average gene expression using pearson correlation analysis. (B) Marker genes for each fibroblasts subset. (C)

Proportion of each fibroblast subset in two groups. (D) GO enrichment analysis of wound fibroblast subtypes. (E) Subclustering of keratinocytes showing 10 subsets; hierarchical clustering of average gene expression using pearson correlation analysis. (F) Proportion of each keratinocytes subset in two groups. (G) Marker genes for each keratinocytes subset.

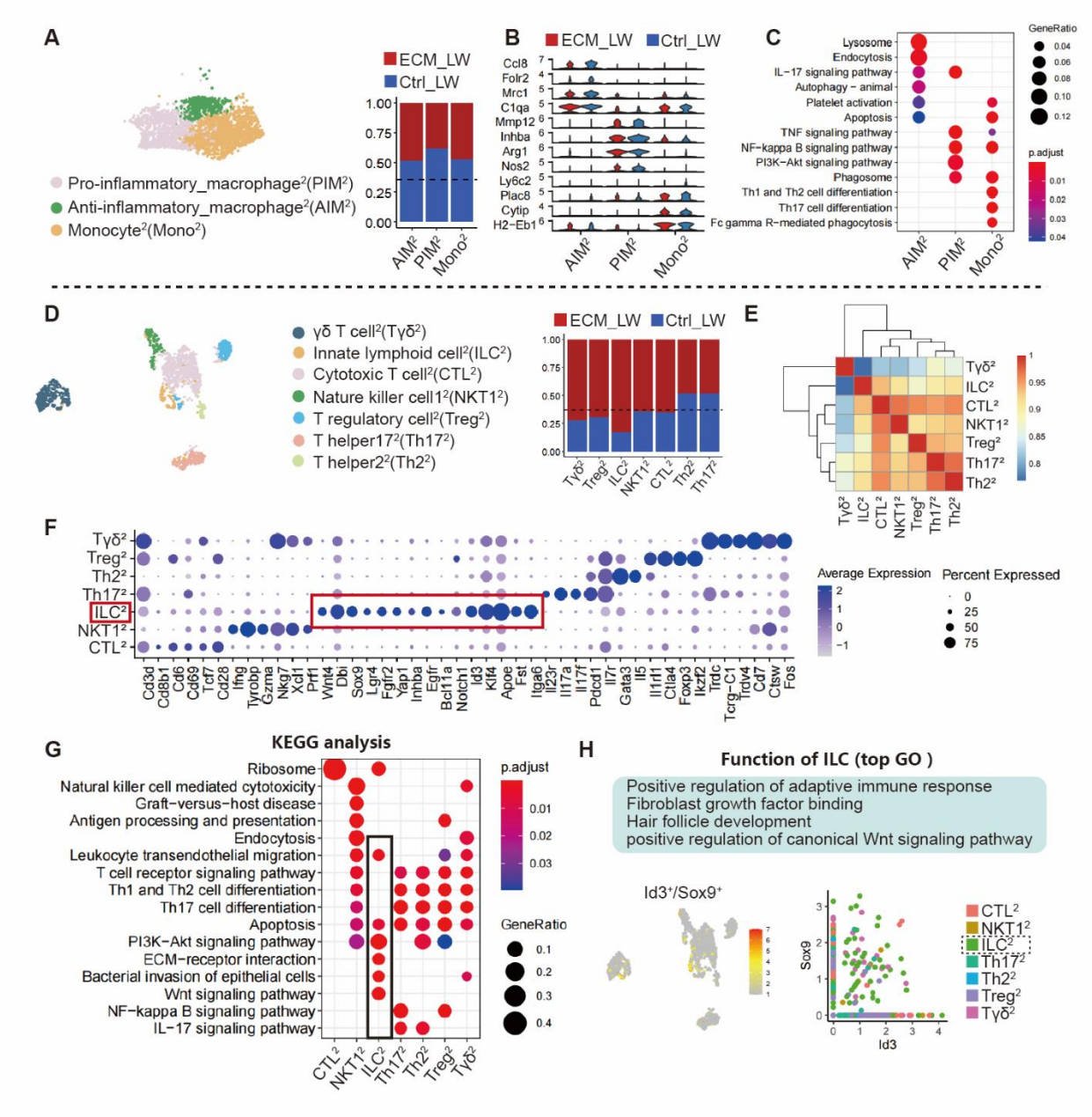

fig. S10. Analysis of immune cells between ECM_LW and Ctrl_LW. (A) Subclustering of MAC showing three subsets and the composition for each subset. (B) Marker genes for each MAC subset and (C) enrichment analysis in KEGG pathway. (D) Subclustering of T cells showing seven subsets and the composition for each subset. (E) Pearson correlation analysis of T cell subsets based on average gene expression. (F) Marker genes for T cell subsets and (G) enrichment analysis of KEGG pathway. (H) GO enrichment analysis of ILC; Overlay of Id3 and Sox9 expression onto the t-SNE space reveals Id3+/ Sox9+ double-positive subclusters.

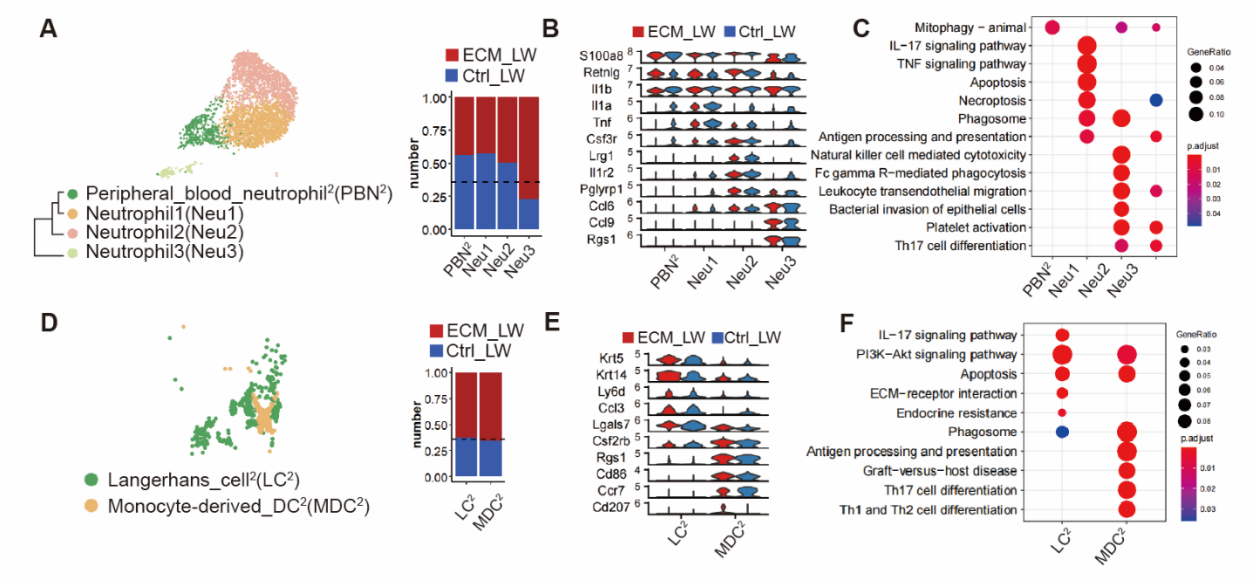

fig. S11. Subclustering analysis of neutrophils and dendritic cells between ECM_LW and Ctrl_LW. (A) Subclustering of neutrophils showing 4 subsets and hierarchical clustering of average gene expression using pearson correlation analysis. The composition for each subset was listed. (B) Marker genes for each neutrophil subset. (C) Gene enrichment analysis of KEGG pathway. (D) Subclustering of dendritic cells showing two subsets and the composition for each subset was listed. (E) Marker genes for each dendritic cells subset. (F) Gene enrichment analysis of KEGG pathway.

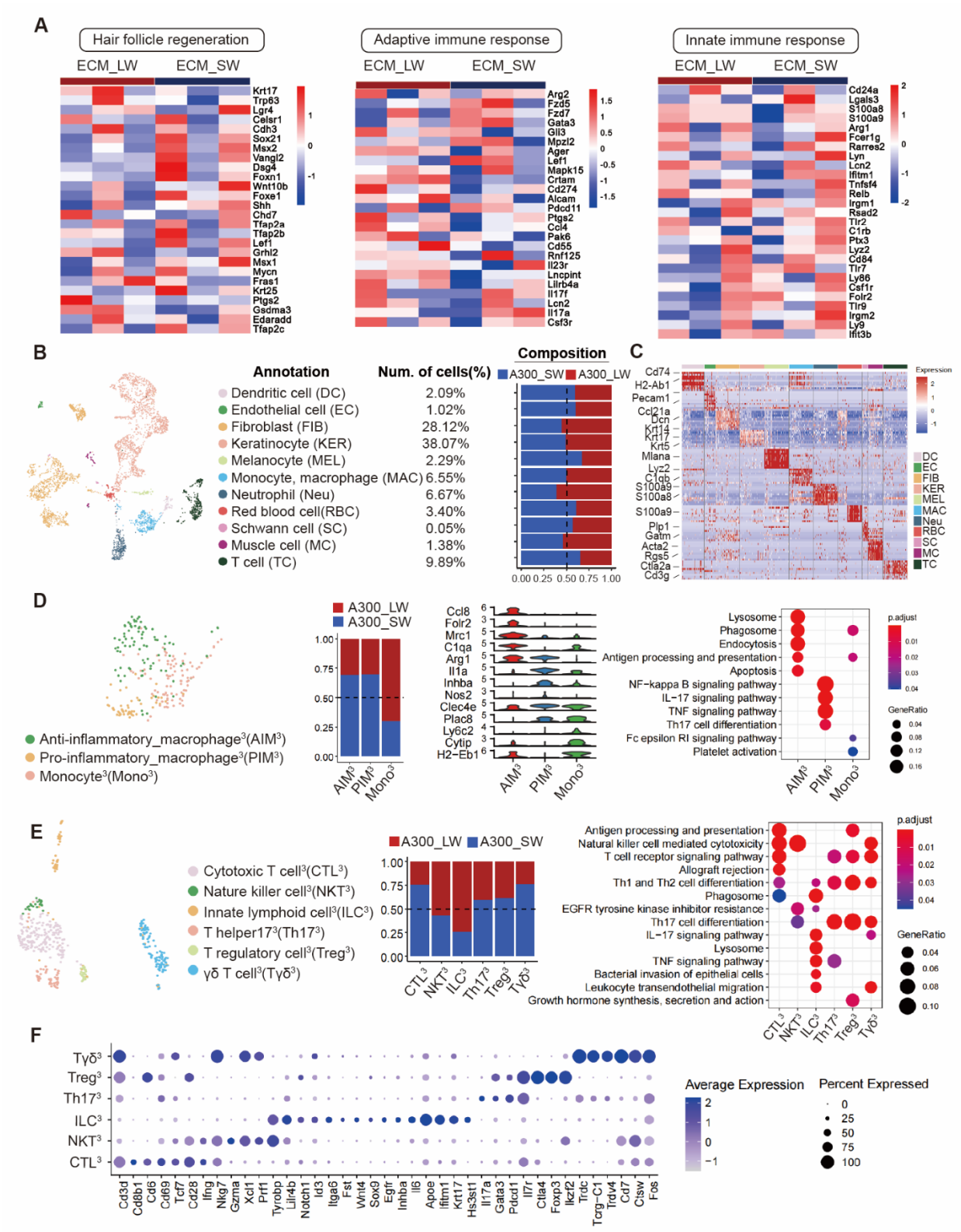
A
Hair follicle regeneration
ECM_LW
ECM_SW
Krt17
Trp63
Lgr4
Celsr1
Cdh3
Sox21
Msx2
Vangl2
Dsg4
Foxn1
Wnt10b
Foxe1
Shh
Chd7
Tfap2a
Tfap2b
Lef1
Grhl2
Msx1
Mycn
Fras1
Krt25
Ptgs2
Gsdma3
Edaradd
Tfap2c
Adaptive immune response
Arg2
Fzd5
Fzd7
Gata3
Gli3
Mpzl2
Ager
Lef1
Mapk15
Crtam
Cd274
Alcam
Pdcd11
Ptgs2
Ccl4
Pak6
Cd55
Rnf125
Il23r
Lncpint
Lilrb4a
Il17f
Lcn2
Il17a
Csf3r
Innate immune response
Cd24a
Lgals3
S100a8
S100a9
Arg1
Fcer1g
Rarres2
Lyn
Lcn2
Ifitm1
Tnfsf4
Relb
Irgm1
Rsad2
Tlr2
C1rb
Ptx3
Lyz2
Cd84
Tlr7
Ly86
Csf1r
Folr2
Tlr9
Irgm2
Ly9
Ifit3b
B
Annotation
Num. of cells(%)
Dendritic cell (DC) 2.09%
Endothelial cell (EC) 1.02%
Fibroblast (FIB) 28.12%
Keratinocyte (KER) 38.07%
Melanocyte (MEL) 2.29%
Monocyte, macrophage (MAC) 6.55%
Neutrophil (Neu) 6.67%
Red blood cell(RBC) 3.40%
Schwann cell (SC) 0.05%
Muscle cell (MC) 1.38%
T cell (TC) 9.89%
Composition
A300_SW
A300_LW
0.00 0.25 0.50 0.75 1.00
C
Cd74
H2-Ab1
Pecam1
Ccl21a
Dcn
Krt14
Krt17
Krt5
Mlana
Lyz2
C1qb
S100a9
S100a8
S100a9
Plp1
Gatm
Acta2
Rgs5
Ctla2a
Cd3g
Expression
DC
EC
FIB
KER
MEL
MAC
Neu
RBC
SC
MC
TC
D
Anti-inflammatory_macrophage3(AIM3)
Pro-inflammatory_macrophage3(PIM3)
Monocyte3(Mono3)
A300_LW
A300_SW
AIM3
PIM3
Mono3
Ccl8
Folr2
Mrc1
C1qa
Arg1
Il1a
Inhba
Nos2
Clec4e
Plac8
Ly6c2
Cytip
H2-Eb1
Lysosome
Phagosome
Endocytosis
Antigen processing and presentation
Apoptosis
NF-kappa B signaling pathway
IL-17 signaling pathway
TNF signaling pathway
Th17 cell differentiation
Fc epsilon RI signaling pathway
Platelet activation
p.adjust
GeneRatio
E
Cytotoxic T cell3(CTL3)
Nature killer cell3(NKT3)
Innate lymphoid cell3(ILC3)
T helper173(Th173)
T regulatory cell3(Treg3)
γδ T cell3(Tγδ3)
A300_LW
A300_SW
CTL3
NKT3
ILC3
Th173
Treg3
Tγδ3
Antigen processing and presentation
Natural killer cell mediated cytotoxicity
T cell receptor signaling pathway
Allograft rejection
Th1 and Th2 cell differentiation
Phagosome
EGFR tyrosine kinase inhibitor resistance
Th17 cell differentiation
IL-17 signaling pathway
Lysosome
TNF signaling pathway
Bacterial invasion of epithelial cells
Leukocyte transendothelial migration
Growth hormone synthesis, secretion and action
p.adjust
GeneRatio
F
Tγδ3
Treg3
Th173
ILC3
NKT3
CTL3
Cd3d
Cd8b1
Cd6
Cd69
Tcf7
Cd28
Ifng
Nkg7
Gzma
Xcl1
Prf1
Tyrobp
Lilr4b
Notch1
Id3
Itga6
Fst
Wnt4
Sox9
Egfr
Inhba
Il6
Apoe
Ifitm1
Krt17
Hs3st1
Il17a
Gata3
Pdcd1
Il7r
Ctla4
Foxp3
Ikzf2
Trdc
Tcrg-C1
Trdv4
Cd7
Ctsw
Fos
Average Expression
Percent Expressed

fig. S12. ScRNA-seq and ST analysis between ECM_SW and ECM_LW. (A) Heatmap showing expression of hair follicle regeneration, adaptive immune response, and innate immune response related genes (bulk seq). (B) Single cells were categorized into 11 main clusters. The number of cell populations in each cluster, number of cells (%), and composition of ECM_LW and ECM_SW groups were listed. (C) Heatmap showed top10 marker genes for each cluster. (D) Subclustering of MAC showing three subsets; The composition for each subset was listed; Marker genes for each MAC subset and enrichment analysis of KEGG pathway. (E) Subclustering of T cells showing seven subsets; The composition for each subset was listed and enrichment analysis of KEGG analysis. (F) Marker genes for T cell subsets.

1. C. Wang *et al.*, The diameter factor of aligned membranes facilitates wound healing by promoting epithelialization in an immune way. *Bioactive materials* **11**, 206-217 (2022).doi:10.1016/j.bioactmat.2021.09.022
2. C. Hu *et al.*, Dissecting the microenvironment around biosynthetic scaffolds in murine skin wound healing. *Science advances* **7**, (2021).doi:10.1126/sciadv.abf0787
3. R. R. Driskell *et al.*, Distinct fibroblast lineages determine dermal architecture in skin development and repair. *Nature* **504**, 277-281 (2013).doi:10.1038/nature12783
4. S. Abbasi *et al.*, Distinct Regulatory Programs Control the Latent Regenerative Potential of Dermal Fibroblasts during Wound Healing. *Cell stem cell* **27**, 396-412.e396 (2020).doi:10.1016/j.stem.2020.07.008
5. B. A. Shook *et al.*, Myofibroblast proliferation and heterogeneity are supported by macrophages during skin repair. *Science (New York, N.Y.)* **362**, (2018).doi:10.1126/science.aar2971
6. C. F. Guerrero-Juarez *et al.*, Single-cell analysis reveals fibroblast heterogeneity and myeloid-derived adipocyte progenitors in murine skin wounds. *Nature communications* **10**, 650 (2019).doi:10.1038/s41467-018-08247-x
7. B. A. Shook *et al.*, Dermal Adipocyte Lipolysis and Myofibroblast Conversion Are Required for Efficient Skin Repair. *Cell stem cell* **26**, 880-895.e886 (2020).doi:10.1016/j.stem.2020.03.013
8. S. Joost *et al.*, The Molecular Anatomy of Mouse Skin during Hair Growth and Rest. *Cell stem cell* **26**, 441-457.e447 (2020).doi:10.1016/j.stem.2020.01.012
9. S. Joost *et al.*, Single-Cell Transcriptomics Reveals that Differentiation and Spatial Signatures Shape Epidermal and Hair Follicle Heterogeneity. *Cell systems* **3**, 221-237.e229 (2016).doi:10.1016/j.cels.2016.08.010
10. Y. Rinkevich *et al.*, Skin fibrosis. Identification and isolation of a dermal lineage with intrinsic fibrogenic potential. *Science (New York, N.Y.)* **348**, aaa2151 (2015).doi:10.1126/science.aaa2151
11. S. B. Telerman *et al.*, Dermal Blimp1 Acts Downstream of Epidermal TGFβ and Wnt/β-Catenin to Regulate Hair Follicle Formation and Growth. *The Journal of investigative dermatology* **137**, 2270-2281 (2017).doi:10.1016/j.jid.2017.06.015

12. D. Haensel *et al.*, Defining Epidermal Basal Cell States during Skin Homeostasis and Wound Healing Using Single-Cell Transcriptomics. *Cell reports* **30**, 3932-3947.e3936 (2020).doi:10.1016/j.celrep.2020.02.091
13. M. W. Hughes *et al.*, Msx2 Supports Epidermal Competency during Wound-Induced Hair Follicle Neogenesis. *The Journal of investigative dermatology* **138**, 2041-2050 (2018).doi:10.1016/j.jid.2018.02.043
14. X. Wang *et al.*, Macrophages induce AKT/β-catenin-dependent Lgr5(+) stem cell activation and hair follicle regeneration through TNF. *Nature communications* **8**, 14091 (2017).doi:10.1038/ncomms14091
15. T. A. Wynn, K. M. Vannella, Macrophages in Tissue Repair, Regeneration, and Fibrosis. *Immunity* **44**, 450-462 (2016).doi:10.1016/j.immuni.2016.02.015
16. K. Sadtler *et al.*, Design, clinical translation and immunological response of biomaterials in regenerative medicine. *Nature Reviews Materials* **1**, 16040 (2016).doi:10.1038/natrevmats.2016.40
17. K. Sadtler *et al.*, Developing a pro-regenerative biomaterial scaffold microenvironment requires T helper 2 cells. *Science (New York, N.Y.)* **352**, 366-370 (2016).doi:10.1126/science.aad9272
18. D. Gay *et al.*, Fgf9 from dermal γδ T cells induces hair follicle neogenesis after wounding. *Nature medicine* **19**, 916-923 (2013).doi:10.1038/nm.3181
19. P. Lee *et al.*, Stimulation of hair follicle stem cell proliferation through an IL-1 dependent activation of γδT-cells. *eLife* **6**, (2017).doi:10.7554/eLife.28875
20. A. Bassez *et al.*, A single-cell map of intratumoral changes during anti-PD1 treatment of patients with breast cancer. *Nature medicine* **27**, 820-832 (2021).doi:10.1038/s41591-021-01323-8
21. B. Z. Qian *et al.*, CCL2 recruits inflammatory monocytes to facilitate breast-tumour metastasis. *Nature* **475**, 222-225 (2012)
22. I. C. Boothby, J. N. Cohen, M. D. Rosenblum, Regulatory T cells in skin injury: At the crossroads of tolerance and tissue repair. *Science immunology* **5**, (2020).doi:10.1126/sciimmunol.aaz9631
23. K. Mok *et al.*, Dermal Condensate Niche Fate Specification Occurs Prior to Formation and Is Placode Progenitor Dependent. *Developmental cell* **48**, 32-48.e35 (2019).doi:10.1016/j.devcel.2018.11.034
24. D. Kim *et al.*, Noncoding dsRNA induces retinoic acid synthesis to stimulate hair follicle regeneration via TLR3. *Nature communications* **10**, 2811 (2019).doi:10.1038/s41467-019-10811-y
25. C. Chu *et al.*, Modulation of foreign body reaction and macrophage phenotypes concerning microenvironment. *Journal of biomedical materials research. Part A* **108**, 127-135 (2020).doi:10.1002/jbm.a.36798
26. Y. Yu *et al.*, Single-cell RNA-seq identifies a PD-1(hi) ILC progenitor and defines its development pathway. *Nature* **539**, 102-106 (2016).doi:10.1038/nature20105
27. P. Bielecki *et al.*, Skin-resident innate lymphoid cells converge on a pathogenic effector state. *Nature* **592**, 128-132 (2021).doi:10.1038/s41586-021-03188-w
28. H. Y. Shih *et al.*, Developmental Acquisition of Regulomes Underlies Innate Lymphoid Cell Functionality. *Cell* **165**, 1120-1133 (2016).doi:10.1016/j.cell.2016.04.029
29. Z. Li *et al.*, Epidermal Notch1 recruits RORγ(+) group 3 innate lymphoid cells to orchestrate normal skin repair. *Nature communications* **7**, 11394 (2016).doi:10.1038/ncomms11394

30. M. Ebbo, A. Crinier, F. Vély, E. Vivier, Innate lymphoid cells: major players in inflammatory diseases. *Nature reviews. Immunology* **17**, 665-678 (2017).doi:10.1038/nri.2017.86
31. D. T. Chang, E. Colton, J. M. Anderson, Paracrine and juxtacrine lymphocyte enhancement of adherent macrophage and foreign body giant cell activation. *Journal of biomedical materials research. Part A* **89**, 490-498 (2009).doi:10.1002/jbm.a.31981
32. B. O. Ode Boni, L. Lamboni, T. Souho, M. Gauthier, G. Yang, Immunomodulation and cellular response to biomaterials: the overriding role of neutrophils in healing. *Materials Horizons* **6**, 1122-1137 (2019).doi:10.1039/C9MH00291J
33. T. Riffelmacher *et al.*, Autophagy-Dependent Generation of Free Fatty Acids Is Critical for Normal Neutrophil Differentiation. *Immunity* **47**, 466-480.e465 (2017).doi:10.1016/j.immuni.2017.08.005